Dynamics of line plumes on horizontal surfaces in turbulent convection

Journal:	*Journal of Fluid Mechanics*
Manuscript ID:	JFM-13-S-0636.R1
mss type:	Standard
Date Submitted by the Author:	30-Jan-2014
Complete List of Authors:	Gunasegarane, G.S.; Indian Institute of Technology Madras, Department of Applied Mechanics Puthenveettil, Baburaj; Indian Institute of Technology Madras, Department of Applied Mechanics
Keyword:	Plumes/thermals < Convection, Turbulent convection < Turbulent Flows, Convection

Accepted for publication in J. Fluid Mech.

Dynamics of line plumes on horizontal surfaces in turbulent convection

G. S. GUNASEGARANE
AND BABURAJ A. PUTHENVEETTIL†

Department of Applied Mechanics, Indian Institute of Technology Madras, Chennai, 600036, India

(Received ?; revised ?; accepted ?. - To be entered by editorial office)

We study the dynamics of line plumes on the bottom horizontal plate in turbulent convection over six decades of Rayleigh number ($10^5 < Ra_w < 10^{11}$) and two decades of Prandtl number or Schmidt number ($0.7 < Pr < 5.3, Sc = 602$). From the visualisations of these plumes in a horizontal plane close to the plate, we identify the main dynamics as (i) motion along the plumes, (ii) lateral merging of the plumes and (iii) initiation of the plumes; various other minor types of motion also occur along with these main dynamics. In quantifying the three main motions, we first find that the spatio-temporal mean velocity along the length of the plumes ($\overline{V_{sh}}$) scales as the large scale flow velocity (V_{LS}), with the fraction of the length of the plumes affected by shear increasing with Ra_w as $L_{ps}/L_p \sim Ra_w^{0.054} Pr^{-0.12}$. The mean time of initiation of the plumes $\overline{t^*}$, scales as the diffusive time scale near the plate, Z_w^2/α, where Z_w is the appropriate length scale near the plate, in agreement with Howard (1964). Merging occurs in a large fraction of the area of the plate, with about 70% of the length of the plumes undergoing merging at $Ra_w \approx 10^{11}$ and $Sc = 602$. The fraction of the length of the plumes that undergoes merging decreases with increase in Ra_w as, $L_{pm}/L_p \sim Ra_w^{-0.054} Pr^{0.12}$; the exponents of Ra_w and Pr being of the same magnitude but of opposite sign as that in the relation for L_{ps}/L_p. Measurements of the locational means of the velocities of merging of the plumes (V_m) show that V_m is a constant during each merging cycle at any location. However, the values of these constant velocities depend on the location and the time of measurement, since the merging velocities are affected by the local shear, which is a function of space and time at any $Ra_w - Pr$ combination. The merging velocities at all Ra_w and Pr have a common lognormal distribution, but their mean and variance increased with increasing Ra_w and decreasing Pr. We quantify the dependence of the spatio-temporal mean merging velocities ($\overline{V_m}$) on Ra_w and Pr, using mass and momentum balance of the region between two merging plumes. $\overline{V_m}$, which are an order lower than $\overline{V_{sh}}$, scale as the entrainment velocity at the sides of the plumes, averaged over the height of the diffusive layer near the plate. This implies that $\overline{V_m}$ scales as the diffusive velocity scale near the plate ν/Z_w. Re_H, the Reynolds number interms of $\overline{V_m}$ and the layer height H scales as $Ra_w^{1/3}$, in the same way as the Nusselt number (Nu) scales approximately; therefore $Re_H \sim Nu$. These relations imply that $Re_w = \overline{V_m} Z_w/\nu$ a Reynolds number near the plate, is an invariant for a given fluid in turbulent convection.

1. Introduction

In turbulent natural convection over horizontal hot surfaces, rising sheets of fluid near the plate show complex dynamics of forming and merging, while being also sheared by

† apbraj@iitm.ac.in

the large scale flow. Since these 'line plumes' transport the major portion of the heat from the plate to the bulk, understanding this dynamics is important to clarify the phenomenology of flux scaling in turbulent convection; improving many technological applications of convection also depend on such an understanding. In addition, the dynamics of these plumes strongly influence the velocity and temperature fields near the plate, whose phenomenology is still not clear. In spite of such importance, the dynamics of these plumes on the horizontal plate have rarely been investigated quantitatively. In the present work we quantify various aspects of the dynamics of line plumes on the bottom horizontal surface in turbulent convection and then propose scaling laws for the predominant dynamics.

Line plumes are formed from the gravitational instability(Pera & Gebhart 1973) of the thin layer of lighter fluid that forms on the hot horizontal plate. Once these line plumes are formed, they rise as sheets while being fed at their base by the local natural convection boundary layers on both sides of the sheets, at the same time moving laterally and merging. After a short distance of rise, they break up into axisymmetric plumes/thermals at heights of the order of 10 times the thermal boundary layer thickness(Zhou & Xia 2010). Line plumes hence collect the fluid near the plate and transport it into the bulk through the ejection of thermals. Motions in the bulk group these thermals; the resultant column of light fluid drives a coherent large scale flow in the bulk. The large scale flow in turn creates a shear near the plate that affects the organisation of these line plumes; the shear also possibly modifies the local natural convection boundary layers on either side of the line plumes (Puthenveettil & Arakeri 2005). Hence at any instant, in the top views of these near-plate coherent structures, a complex pattern of lines is seen due to the combined effect of the spatial nature of the boundary layer instability, the spatially varying external shear due to the large scale flow and, more importantly, due to the interaction between these line plumes.

Such complex plume structures, look geometrically quite different at different Rayleigh numbers (Ra) and Prandtl numbers (Pr), and have their mean and integral properties strongly dependent on Ra and Pr. Here, $Ra = g\beta\Delta T H^3/\nu\alpha$ and $Pr = \nu/\alpha$, with g being the acceleration due to gravity, β the coefficient of thermal expansion, ΔT the temperature difference across the fluid layer, H the height of the fluid layer, ν the kinematic viscosity and $\alpha = k/\rho C_p$ the thermal diffusivity with k the thermal conductivity, ρ the density and C_p the specific heat at constant pressure. To describe the phenomena near the plate it is also convenient to define a Rayleigh number based on the temperature drop near the plate ΔT_w, as

$$Ra_w = g\beta\Delta T_w H^3/\nu\alpha. \tag{1.1}$$

For Rayleigh-Bénard convection (RBC), at high Ra, since $\Delta T_w = \Delta T/2$, $Ra_w = Ra/2$.

One of the mean properties of these plume structures at any instant, the mean plume spacing $\overline{\lambda}$, was shown to be proportional to,

$$Z_w = \left(\frac{\nu\alpha}{g\beta\Delta T_w}\right)^{1/3} = \frac{H}{Ra_w^{1/3}}, \tag{1.2}$$

the appropriate length scale obtained by a balance of buoyant and diffusive processes near the plate by Theerthan & Arakeri (1998); Puthenveettil & Arakeri (2005). Dependence of other mean geometric properties of these line plumes on Ra have also been obtained empirically by Zhou & Xia (2010). Puthenveettil *et al.* (2011) (herein after referred as PA11) obtained relations for an integral property of these plume structures, viz. the total length L_p, under the assumption that natural convection boundary layers, or equivalently

line plumes that are an outcome of these boundary layers, carry most of the heat from the plate to the bulk. The plume lengths per unit area $L_p/A \sim 1/Z_w$ for any given fluid; a similar $Ra^{1/3}$ dependence were also observed by Bosbach *et al.* (2012), eventhough they interpreted it differently. This result also implied that $L_pH/A \sim Nu$, the Nusselt number; $Nu = Q/(k\Delta T/H)$, where Q is the heat flux.

Even though the mean and the integral properties of the plume structures are strong functions of Ra and Pr, the statistical distributions of the properties of these structures are not. Puthenveettil & Arakeri (2005) found that the probability distribution function (pdf) of the spacings between these line plumes showed a common log-normal form at different Ra and Pr; Haramina & Tilgner (2004) have tried to explain such a distribution. A similar common log-normal distribution has been found for other geometric properties of these line plumes by Zhou & Xia (2010). These plume structures also had a common multifractal spectrum associated with them over a decade of Ra (Puthenveettil, Ananthakrishna & Arakeri 2005), implying that the probability of occurrence of the line plumes in any area of the planform is independent of Ra. The common form of the pdfs observed by various researchers and the common multifractal spectrum point towards some commonality in the underlying dynamics by which these planforms are formed.

Spangenberg & Rowland (1961) was the first to qualitatively describe the dynamics of these structures at the free surface in evaporative convection; they identified the transient nature of forming, random motion and plunging down of line plumes. Husar & Sparrow (1968) also made similar qualitative observations while studying the patterns of line plumes on a hot horizontal plate with no side walls. The first quantitative measurements of the horizontal velocities of these line plumes on the bottom plate, which they considered as waves on the viscous boundary layer, was by Zocchi *et al.* (1990). In their visualisations, the line plumes mostly moved lateral to their length, in the direction of the large scale flow; the velocity distribution was asymmetric with a long tail, whose peak was approximately same as the velocity of the large scale flow. Funfschilling & Ahlers (2004) qualitatively saw motion along the length of the plumes and studied the azimuthal oscillations of this motion. Recently, Hogg & Ahlers (2013) have estimated the mean and fluctuating horizontal velocities in the convection cell using spatial correlation of shadowgraph images obtained from the top view of the cell. Since plumes near the plate are the predominant structures seen in such images, the obtained velocities are mostly the plume velocities. Hogg & Ahlers (2013) obtained the scaling of the mean and the fluctuating velocity to be the same as that of the large scale flow. The magnitude of the mean velocities were two orders lower than that of the bulk flow while the magnitude of fluctuating velocities were of the same order as that of the bulk flow.

Most of the above investigations of the dynamics of these line plumes on the plate have been qualitative. The few quantitative investigations fail to describe the whole gamut of motions and identify the predominant dynamics as that of the large scale flow. However, as described above, the line plumes have various other motions other than that due to the large scale flow alone. The motion of these line plumes, that have a higher temperature than in the bulk, contribute to the velocity and temperature profiles near the plate in turbulent convection. Since various theoretical expressions for these profiles have been proposed by Theerthan & Arakeri (1998), Shishkina & Thess (2009) and Ahlers *et al.* (2012), understanding the quantitative details of the dynamics of line plumes is crucial to understand the origin of the profiles of temperature and velocity near the plate. Such profiles near the plate, based on realistic phenomenology of the dynamics near the plate, could result in better wall functions for modelling turbulent convection computationally. More importantly, since line plumes transport most of the heat from the plate (Shishkina & Wagner 2008), understanding the dynamics of these structures is necessary to clarify

the phenomenology of heat transport in turbulent convection. Such knowledge will also be of great use in applications that use natural convection heat transport like electronic cooling, materials processing and atmospheric modelling. In spite of such importance, to the best of our knowledge, details of the dynamics of line plumes on the hot plate in turbulent convection are still unexplored. There is no information available about the various types of motion, the predominant ones from these types, the relative magnitude of the predominant motions with the other velocity scales in turbulent convection and the scaling of the predominant motions with Ra and Pr; the present paper focusses on these aspects for the first time.

We study the different types of dynamics of line plumes on the bottom plate in turbulent convection over horizontal surfaces using three experimental setups that use air ($Pr \approx 0.7$), water ($Pr \approx 3.6$ to 5.3) and concentration driven convection in water with Schmidt number, $Sc = \nu/D = 602$, where D is the molecular diffusivity, to achieve a wide range of Pr and Rayleigh numbers ($10^5 < Ra_w < 10^{11}$). Evolution of the line plume structure with time in a horizontal plane close to the bottom plate are obtained to qualitatively identify a range of dynamics for the first time; shear, initiation and merging of plumes are found to be the predominant types of motions, other rare, miscellaneous dynamics are also classified. It is shown that the scaling laws for the mean longitudinal velocities along the plumes and the mean initiation times of the plumes are, respectively, to be the same as that for the large scale flow and that proposed by Howard (1964). We then focus on quantitatively describing the merging motion of the plumes, since this motion has not been studied quantitatively so far. After showing the relative magnitudes of merging and longitudinal motion, in terms of the length of plumes affected by these, we show for the first time that all plumes merge with a constant velocity during their merging cycle, eventhough the value of this velocity depends on the location, as well as on the Ra_w and Pr. We discover that the statistics of the merging velocities from planforms, collected from different locations at different times, show a common log-normal distribution at all Ra_w and Pr, while the mean increases with increase in Ra_w and decrease in Pr. We then, for the first time, develop a scaling theory for the behaviour of mean merging velocities to show that the mean merging velocities are proportional to the diffusive velocity scale near the plate.

The paper is organised as follows. The description of the experimental setups is given in § 2, the qualitative description of the dynamics in § 3 and the methodology of the measurements in § 4. The scaling of longitudinal velocities is described in § 5.1 while that of initiation times in § 5.2. § 5.3.1 discusses the fraction of plume length over which merging is predominant, while § 5.3.2 discusses the variation of merging velocities over a merging cycle. The statistics of merging velocities are discussed in § 5.3.3 and the mean merging velocities described in § 5.3.4. The theory for the scaling of mean merging velocities is then developed in § 6.

2. Experiments

The dynamics of plumes near the plate were obtained from top view images in experiments conducted at $Pr = 0.74, 3.6$ to 5.3 and $Sc = 602$. We briefly discuss the setups and the procedures used for these three types of experiments in this section; details could be found in Gunasegarane (2014). The details of the values of the parameters used in these experiments are given in table 1.

Pr or Sc	H(mm)	A_p(mm^2)	ΔT_worΔC_w	$Flux$	Ra_w	$\bar{\lambda}'$(mm/s)
0.74	500	2500×500	10.48	19.12	1.287×10^8	16.16
			15.46	31.44	1.766×10^8	19.132
			20.17	44.16	2.183×10^8	20.64
			24.89	57.64	2.542×10^8	21.886
5.3	50	300×300	0.05	65	1.31×10^5	0.2608
5.3			0.15	190	3.92×10^5	0.3922
5.2			0.26	260	7.32×10^5	0.4758
5.1			0.56	585	1.66×10^6	0.5776
5.1			1.12	1040	3.225×10^6	0.7440
4.9			2.03	1625	6.464×10^6	0.8630
4.7			2.53	2340	8.49×10^6	0.9496
3.9			4.65	4158	2.137×10^7	1.2741
5.3	100	300×300	0.15	50	3.14×10^6	0.3866
5.2			0.85	260	1.91×10^7	0.6726
5.1			1.19	585	2.83×10^7	0.7292
4.7			2.66	1625	7.145×10^7	1.0448
4.0			3.19	2340	1.11×10^8	1.1044
5.3	150	300×300	0.21	50	1.48×10^7	0.4666
5.0			1.87	585	1.57×10^8	0.9297
4.7			2.92	1625	2.65×10^8	1.1048
4.0			3.26	2340	3.82×10^8	1.1180
3.6	200	300×300	5.41	4158	1.77×10^9	1.2772
5.3	210	300×300	0.23	50	4.46×10^7	0.4498
5.1			2.45	1040	5.39×10^8	0.9818
4.0			4.91	2340	1.58×10^9	1.222
3.6			5.98	4158	2.27×10^9	1.3132
602	230	100×100	1	0.021	6.39×10^{10}	0.15
			2.65	0.09	1.667×10^{11}	0.2094
			3.21	0.1116	2.034×10^{11}	0.216

TABLE 1. Values of parameters for the planforms from which the plume dynamics were measured. For concentration driven convection at $Sc = 602$, the driving potential ΔC_w is in gl^{-1} and flux in mg cm^{-2} min^{-1} while for other cases it is in ^{o}C and W m^{-2}. H is the liquid layer height and A_p is the plate area.

2.1. $Pr = 0.74$

The schematic of the convection cell used at $Pr = 0.74$, that had an area of cross section 2m×0.5m, with air confined between top and bottom aluminium plates, is shown in figure 1(a). The aluminium plates were separated by four transparent polycarbonate side walls of height 0.5m. The bottom aluminium plate was maintained at a constant temperature using a temperature controlled water circulating system. The top plate was air cooled by fans so that a constant mean temperature difference ΔT between the plates could be maintained. ΔT was determined from spatial and temporal averaging of the plate temperatures recorded at 25 locations in each plate using PT100 resistance temperature detectors. The range of Rayleigh numbers in these experiments, $1.28 \times 10^8 < Ra_w < 2.54 \times 10^8$, was obtained by changing ΔT. Each experiment was run for approximately 300 minutes to ensure a steady state condition inside the convection cell before measurements were taken. The planforms of plume structures near the plate were made visible when a horizontal light sheet from a 532 nm Nd-Yag laser was scattered by the smoke particles mixed with the air inside the convection cell. The laser sheet was 2mm thick with its

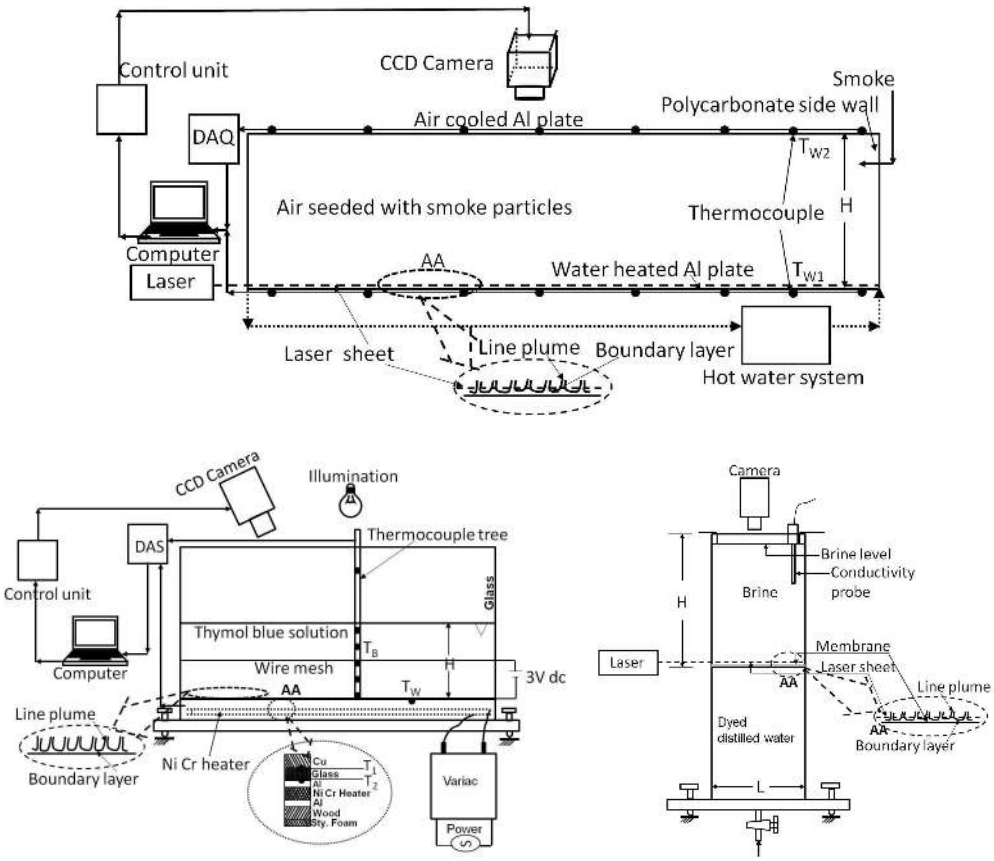

FIGURE 1. Schematic of the experimental setups used for studying; (a), steady temperature driven convection in air at $Pr = 0.74$; (b), unsteady temperature driven convection in water at $Pr = 3.6$ to 5.3 and (c), quasi-steady concentration driven convection at $Sc = 602$ (Puthenveettil & Arakeri 2005).

centreline at $h_m = 4$mm above the bottom hot plate. Since the plumes have relatively lesser number of smoke particles, they scatter less light and hence appear as dark lines in a bright background. Figure 2(a) shows one such top view of the plume structures near the plate at $Ra_w = 2.54 \times 10^8$, the dark lines in the figure are the top view of the rising line plumes near the bottom plate. The convection cell had a closed opaque top, the top views of the plume structures near the bottom plate were hence captured through the side walls by a CCD camera at 10fps. The perspective errors caused by this inclined camera axis were removed using a horizontal calibration plate in the plane of observation.

2.2. $Pr = 3.6 - 5.3$

The plume structures near the plate in water for $1.31 \times 10^5 < Ra_w < 2.27 \times 10^9$ at $3.6 < Pr < 5.3$, were obtained from unsteady temperature driven convection experiments conducted in a convection cell of size 30cm $\times$30cm $\times$25cm, the schematic of which is shown in figure 1(b). The top of the convection cell was kept open to ambient while the bottom copper plate was used to provide a constant heat flux. The constant heat flux was provided by a Nichrome wire heater connected to variac, sandwiched between two aluminium plates in a vertical plate array as shown in figure 1(b). The temperature

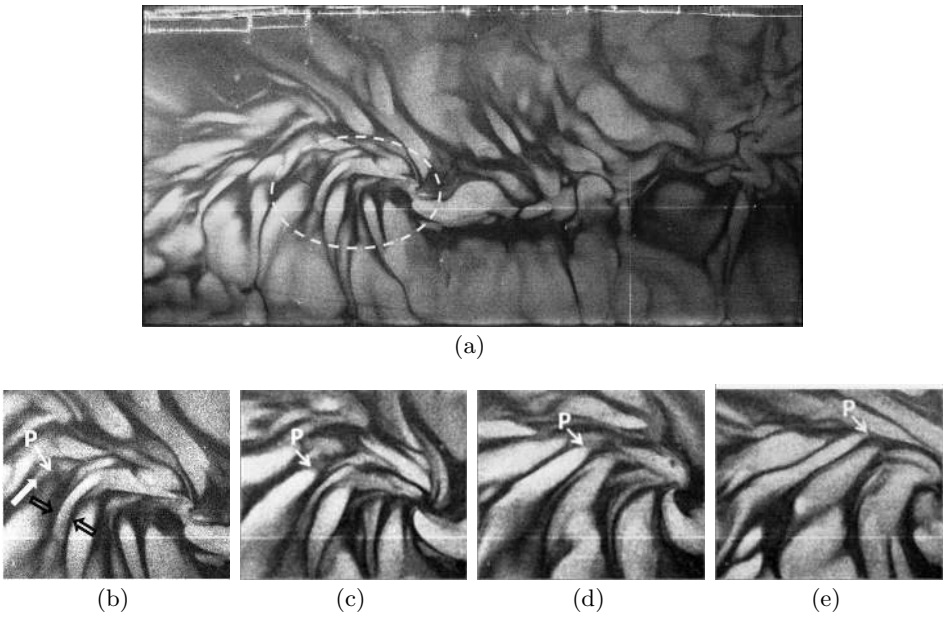

FIGURE 2. Dynamics of plumes in a shear dominant region at $Pr = 0.74$, and $Ra_w = 2.54 \times 10^8$; (a), the instantaneous planform in half the cell area of size 985mm×477mm; (b)-(e), merging sequence in the marked region in (a) that has dominant local shear. The filled arrow in (b) shows the direction of shear, inferred from the motion of the point marked as P. The hollow arrows show the direction of merging. The zoomed images are of size 162mm×135mm separated by 0.5s.

difference $(T_1 - T_2)$, measured across the glass plate in this vertical array of plates was used to estimate the flux supplied to the bottom plate. This flux was also cross checked with the heat flux supplied by the nichrome wire, estimated from the resistance of the wire and the voltage input. The glass side walls as well as the bottom of the cell were sufficiently insulated to minimise the heat loss. The temperature difference between the bottom plate and the bulk fluid $T_w - T_B = \Delta T_w$, was measured by T type thermocouples, the precision limit of the thermocouples was 0.02°. Except for the measurement at $\Delta T = 0.05°$ the possible error in temperature measurement was of the order of 10%. The experiments were conducted in a temperature controlled laboratory so that environmental temperature fluctuations were minimal. Even though the temperature of the bottom plate T_w and the bulk fluid T_B increased with time, a constant ΔT_w was obtained after about 200 min due to the balance of influx and efflux of heat. The maximum deviation of ΔT_w from the mean was 3.46 %, observed for experiments at $Ra_w = 1.31 \times 10^5$. Assuming no error in other quantities, the corresponding error in Ra_w is about 4%, which is negligible. Hence, since the dynamics near the plate is solely determined by the driving potential ΔT_w and Pr, the results from the present unsteady experiments could be compared to that from steady RBC.

When a 5V DC supply is applied across the water layer, the local pH of water near the cathodic bottom plate changes due to accumulation of H^+ ions. Due to this pH change, the thymol blue dye added to the water changes its colour near the bottom plate, thereby making the plume structures near the plate visible (Baker 1966). Since the change in pH occurs in regions close to the bottom plate alone, only the plume structures very near the plate are seen by this technique. The expected plane of visualisation is approximately between the thermal and velocity natural convection boundary layer thicknesses, see

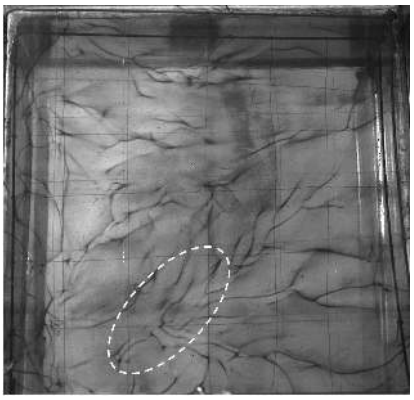

(a)

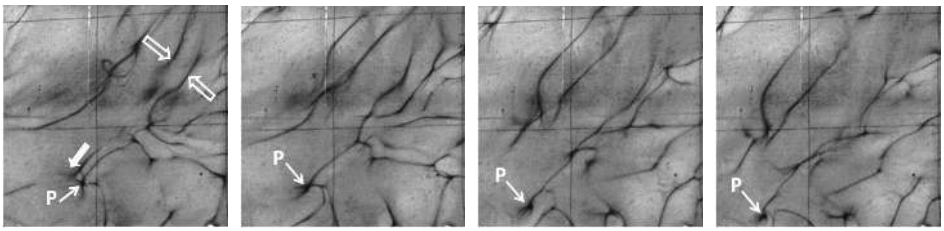

(b) $t = 0$ s (c) $t = 5$ s (d) $t = 10$ s (e) $t = 13$ s

FIGURE 3. Dynamics of plumes in a shear dominant region at $Pr = 4.7$, and $Ra_w = 2.65 \times 10^8$; (a), the instantaneous planform of the entire cell area of size 298mm×287mm; (b)-(e), merging sequence in the marked region in (a) that has dominant local shear. The filled arrow in (b) shows the direction of shear, inferred from the motion of point marked as P. The hollow arrows show the direction of merging. The zoomed images are of size 100mm×77mm.

Appendix A for details. The dark lines seen in figure 3(a) are the line plumes observed near the plate using this technique.

2.3. $Sc = 602$

Figure 1(c) shows the schematic of the experimental set up used by Puthenveettil & Arakeri (2005) for unsteady concentration driven convection at $Sc = 602$ that occurred in a layer of brine placed over a layer of water separated by a horizontal membrane. The experiments were conducted in a tank of cross section 10cm×10cm for a liquid layer height of $H = 23$cm. The plume structure shown in figure 4(a) was observed when an Ar-ion laser (488nm) sheet, at $h_m = 3$mm above the membrane, intercepted the line plumes that had sodium fluorescein dye in them. The membrane acted in a way similar to the bottom plate in temperature driven convection, allowing only diffusive transport of mass across it. Since the time scale of dynamics of line plumes near the membrane in this system was much lower than the time scale of variation of flux and the large scale flow, the convection was quasi-steady (Puthenveettil & Arakeri (2008) and Ramareddy & Puthenveettil (2011)). The results could hence be compared with steady RBC when the concentration difference ΔC_w in Ra_w is calculated using the concentration difference above/below the membrane. The reader is referred to Puthenveettil & Arakeri (2005), Puthenveettil & Arakeri (2008) and Ramareddy & Puthenveettil (2011) for more details of the set-up and procedure.

For all the three types of experiments, the vertical location of the plane of measurement

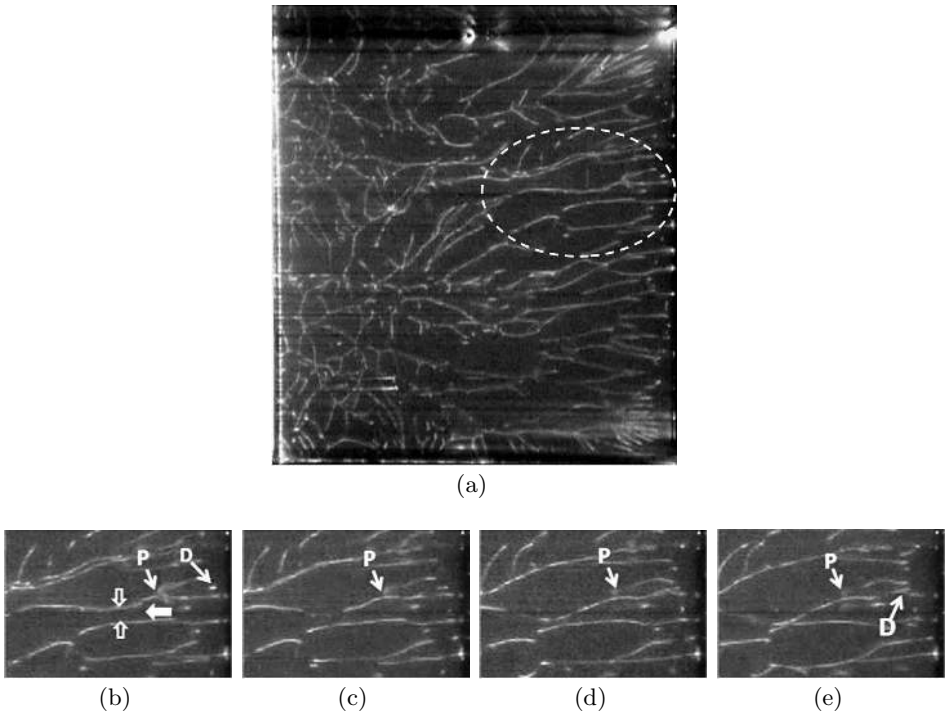

(a) (b) (c) (d) (e)

FIGURE 4. Dynamics of plumes observed by Puthenveettil & Arakeri (2005) in a shear dominant region at $Sc = 602$, and $Ra_w = 2.034 \times 10^{11}$; (a), the instantaneous planform of the entire convection surface of the cell of size 87mm×98mm; (b)-(e), merging sequence in the marked region in (a) that has dominant shear. The filled arrow in figure(b) shows the direction of shear, inferred from the motion of P. The unfilled arrows show the direction of merging. The zoomed images are of size 34mm×23mm separated by 2s.

with respect to the boundary layer thicknesses and the effect of a fixed vertical location of the plane of visualisation on the observed dynamics, when the boundary layer thickness change with Ra_w is discussed in Appendix A.

3. Qualitative description of dynamics

The videos of the topviews of the plume dynamics were studied to classify the complex dynamics of these plumes into the following four classes, (i) longitudinal motion of line plumes, (ii) lateral motion of line plumes, (iii) initiation of point plumes and (iv) miscellaneous motions.

We now qualitatively describe the first three classes of motion in this section before quantifying them in § 5. A qualitative description of of the miscellaneous motions is given in Appendix B.

3.1. *Longitudinal motion of line plumes*

There was substantial motion along the lengths of plumes in various regions of the planforms. Most often, these motions along the length of the plumes also coincided with the direction of local alignment of the plumes. Such an instance of motion is seen in Figures 2(b) to 2(e) at $Ra_w = 2.54 \times 10^8$ and $Pr = 0.74$. The point P in the figure, which indicates the point of joining of two plumes, moves along the length of the plumes on both sides of P. The plumes to the bottom left of P are also aligned along the direction

of motion of P. From such a motion we infer that there is a shear in the planform along the diagonal connecting bottom left to top right of these images. This direction of shear is shown by a filled arrow in figure 2(b). At any instant, at a given Ra_w and Pr, there were regions with shear and without shear on the planforms, the latter usually seen close to the side walls and at points were plumes formed rising columns. However, even at a given Ra_w and Pr, the locations of regions with and without shear were not constant due to the shifts in the direction of the large scale flow. Hence, we would often see shear dominant regions expanding or shifting to shear free regions in time and vice versa, visible by shifting regions of aligned plumes; point P in figure 2(b) seems to be at the edge of such a region.

The plumes, that are aligned along the direction of shear, also merge with time, as is obvious by observing the space between the plumes indicated by the hollow arrows in figure 2(b). Such dynamics that include motion of plume features along their lengths, aligning of plumes along this direction of motion and the merging of such parallel plumes could also be seen in figures 3(b) to 3(e) at a similar Ra_w of 2.65×10^8 but at a higher Pr of 4.7. Comparing the motion of point P in figures 3(b) to 3(e) with that in figures 2(b) to 2(e) we could infer that the velocity of longitudinal motion of the plumes are substantially less for the higher Pr case. A qualitatively similar dynamics in the shear dominant region at a much higher Ra_w of 2.034×10^{11} and Sc of 602 is shown in figures 4(b) to 4(e). A similar comparison of the motion of P between figures 3(b) to 3(e) with that in 4(b) to 4(e) does not show a substantial difference in velocities of longitudinal motion, even though the Pr is much higher in the latter set of planforms. As we quantify later in § 5.3.1, the strength of longitudinal motion is also a strong function of Ra_w, which being substantially higher for figure 4, offsets the decrease due to a higher Pr.

3.2. *Lateral motion of line plumes*

Pairs of line plumes that are near to each other and nearly parallel were observed to move perpendicular to their length and merge. Such a motion could be seen in figures 5(b) to 5(e), which shows the progressive zoomed views of the region marked by the dashed ellipse in the planform in figure 5(a) at $Ra_w = 2.54 \times 10^8$ and $Pr = 0.74$. The lateral merging is obvious from the reducing distance between the line plumes indicated by the hollow arrows in these images. Similar lateral merging at around similar $Ra_w = 2.65 \times 10^8$ but at a higher $Pr = 4.7$ in water is shown in figures 6(b) to 6(e). The merging sequence of two nearby plumes in the concentration driven experiments at a higher $Ra_w = 2.034 \times 10^{11}$ and a higher $Sc = 602$, than the case of water is seen in figures 7(b) to 7(e). As we show later in § 5.3.1, these merging motions are the predominant dynamics of these line plumes at lower Ra_w and higher Pr.

The lateral merging of plumes occurred in all the regions in a planform that had different strengths of shear. However, the plumes were observed to merge faster in the low shear regions than in the high shear regions at any Ra_w and Pr. Further, at any Ra_w and Pr, the number of merging instances were also observed to be lower in high shear areas compared to the low shear areas. In both such regions the velocities of merging were observed to increase with increase in Ra_w or decrease in Pr. Due to the presence of large shear in some regions, or due to the absence of nearby plumes in some other regions, the total length of plumes in the planform does not undergo lateral merging. At any Ra_w and Pr, there is hence a fraction of the total plume length in the planform that undergoes merging. Further, we also notice that plumes have to be close to each other to undergo merging, else they remain stationary or are swept away by the large scale flow.

The merging of nearby plumes were not limited to only when they were parallel. Often, one end of nearby plumes would be touching each other with the distance between the

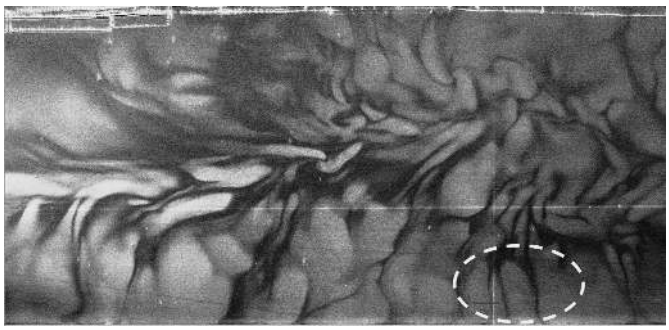

(a)

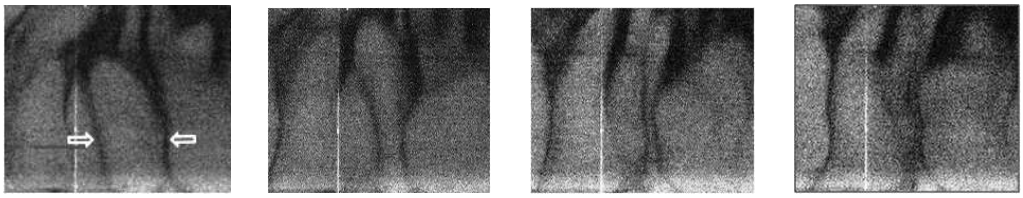

(b) (c) (d) (e)

FIGURE 5. Dynamics of plumes in a low shear region at $Pr = 0.74$ and $Ra_w = 2.54 \times 10^8$; (a), The instantaneous planform in half the cell area of size 985mm×477mm; (b) to (e), merging sequence in a region of size 162mm×135mm that has negligible shear, marked with a dashed ellipse in (a). The images (b) to (e) are separated by $0.4s$.

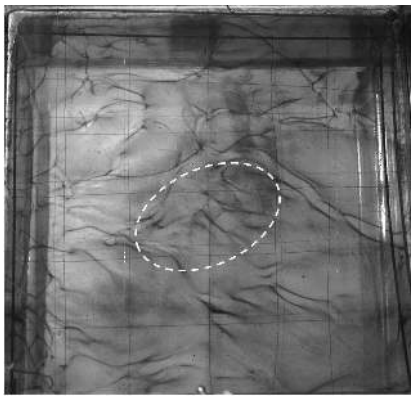

(a)

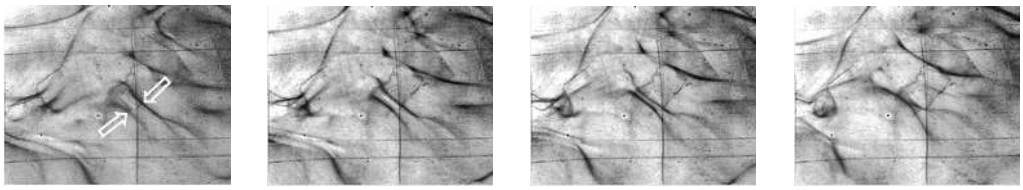

(b) $t = 0$ s (c) $t = 1.5$ s (d) $t = 3$ s (e) $t = 5$ s

FIGURE 6. Dynamics of plumes in a low shear region at $Pr = 4.7$, and $Ra_w = 2.65 \times 10^8$; (a), the instantaneous planform of the entire cell area of size 298mm ×287mm; (b) - (e), merging sequence in the marked region in (a) with negligible shear; The images are of size 100mm ×77mm.

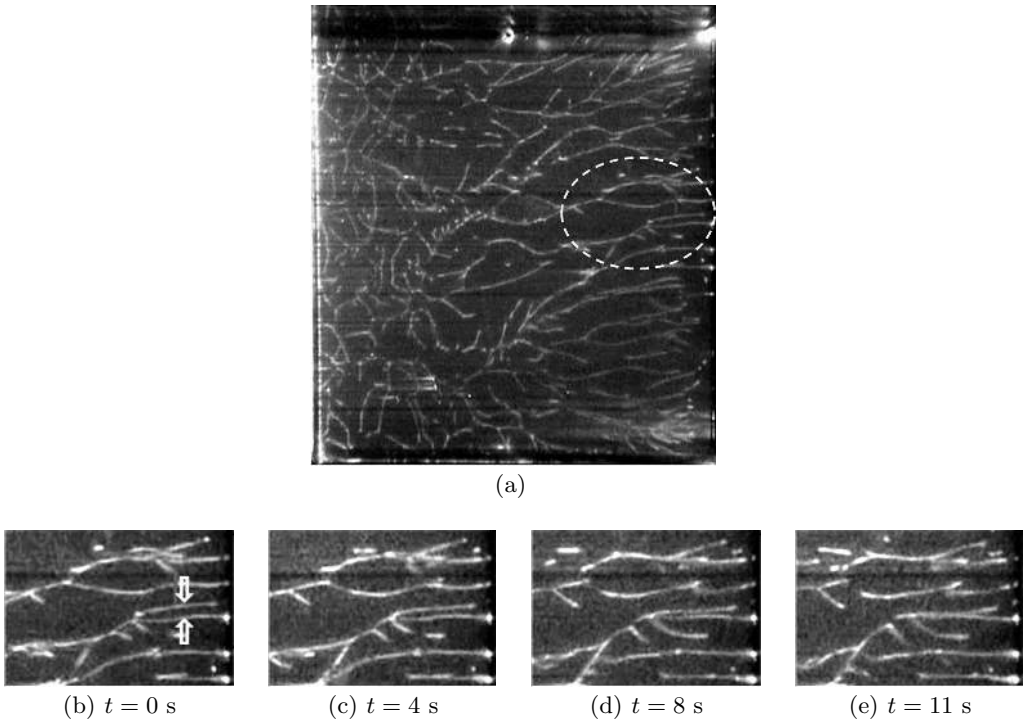

(a) (b) $t = 0$ s (c) $t = 4$ s (d) $t = 8$ s (e) $t = 11$ s

FIGURE 7. Dynamics of plumes observed by Puthenveettil & Arakeri (2005) at $Sc = 602$ and $Ra_w = 2.034 \times 10^{11}$; (a), The instantaneous planform of the entire convection surface of the cell of size 87mm×98mm; (b) to (e), zoomed views of size 34mm×23mm of the merging plumes in the region showed by the dashed ellipse in (a).

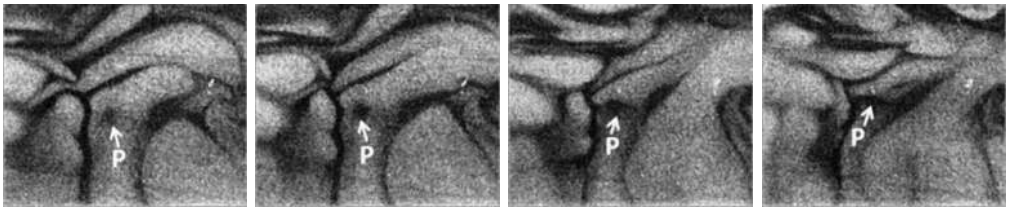

(a) (b) (c) (d)

FIGURE 8. Sequence of images showing the dynamics of initiation and elongation of line plumes at $Ra_w = 2.54 \times 10^8$ and $Pr = 0.74$. The point P shows the initiation of a line plume. The images are of size 171mm×135mm and are separated by 0.2 s.

plumes increasing as we go away from the contact point. These plumes also merge in such a condition, often becoming parallel during the merging process (see figures 4(b) to 4(e) for plumes touching at P and 7(b) to 7(e)). Often, since there are more than a pair of plumes that are nearby to each other, merging of a pair would also result in this pair of plumes moving away from nearby plumes, we however do not classify this as a separate motion since the motion is again due to the merging.

3.3. *Initiation of plumes*

The third class of motion that we observe often is the initiation of new plumes in regions that have become free of plumes due to their motions. Figure 8 shows the sequence of initiation of a plume in a region free of plumes at $Ra_w = 2.54 \times 10^8$ and $Pr = 0.74$.

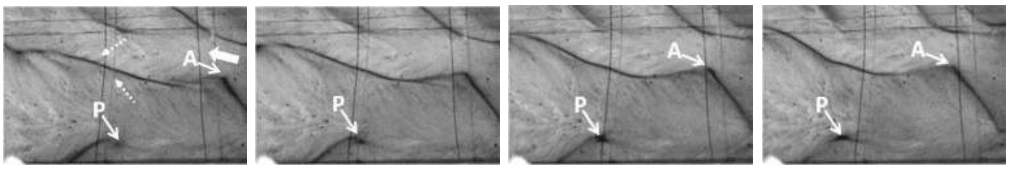

(a) (b) (c) (d)

FIGURE 9. Dynamics of initiation and elongation of line plumes at $Pr = 4.7$, and $Ra_w = 2.65 \times 10^8$. Point P shows the location of initiation. The dashed arrows show the direction of motion in the boundary layers between the plumes. The images are of size 98mm×65mm and are separated by 1.5s. The filled arrow in (a) shows the direction of shear inferred from the motion of A.

The initiation occurs as a point burst on the underlying boundary layer, shown by point P in figure 8(a). This point plume is soon elongated in the direction of the prevalent shear in the region at which it is initiated (see figures 8(b) to 8(d)). The prevalent shear at this point could be due to the entrainment flow field of a nearby plume, or it could be due to the external shear by the large scale flow. In the former case the elongation is often approximately at right angles to the nearby plume; figure 8 is an example of such elongation. The initiation dynamics at a larger Pr of 4.6 at around the same Ra_w as in figure 8 is shown in figure 9. The filled arrow shows the predominant shear field near point P in these figures, as inferred from the motion of point A in the figures. The shear is mostly due to the large scale flow since the plumes are seen to be aligned in this direction, the point plume also elongates in the direction parallel to the nearby plumes. The initiation dynamics at the location marked by D in figures 4(b) to 4(e) at a much larger Sc of 602 and at a higher Ra_w of 2.043×10^{11} shows the influence of both the external shear and the nearby plumes. The initial elongation of the plume is along the direction in which the nearby plumes are aligned, parallel to the nearby plumes, and hence is mostly due to the external shear. However at later stages, the orientation of the plume changes so as to join the nearby plume at an angle, possibly due to the influence of the nearby plume. By comparing the size of the initiation plume at the three different Pr in figures 8, 9 and 4 we could see that the initiation occurs as a smaller, sharper point with increase in Pr. In addition, the elongation also appears to be slower with increase in Pr.

The motions described in § 3.1 to § 3.3 are the predominant motions of the line plumes which we quantified using the measurements described in the next section. However, in addition to these motions, the plumes also undergo miscellaneous types of motions that occur not so frequently; such motions are described in Appendix B.

4. Measurement of plume dynamics

We undertake the following five measurements to quantify the three predominant dynamics described in § 3. All these measurements are made on top view images, similar to that shown in figures 2 to 9.

(*a*) The displacement of features along the plume as a function of time at different locations, to estimate the locational means of the longitudinal velocities along the line plumes (V_{sh}).

(*b*) The spacing (λ) between two line plumes that are nearly parallel as a function of time at different locations, to estimate the locational means of merging velocities V_m.

(*c*) The time of initiation of point plumes t^* at different locations.

(d) The total length of plumes in a planform over which there is substantial longitudinal motion (L_{ps}).

(e) The total length of plumes in a planform that merge (L_{pm}).

4.1. *Displacement of features along plumes*

The velocities along the length of the plumes were calculated by measuring the speed at which some feature of the plume moves along the plume. The features chosen were not some separate structure distant from the plume, but structures on the plumes themselves like a thicker/thinner region, a tip of the plume, a bend in the plume a joint of one plume to another or just a change in intensity on a plume which could be identified. Further, the features were only chosen in regions where they move along the motion in the plume, as observable qualitatively due to shift in intensities or specks along the plume. The displacement of a feature, similar to the dot marked by P in figures 3(b) to 3(e), along the plume length in successive frames of an image sequence is measured. The feature is tracked over a time period of 1.5 to 13 s which is much lower than H/V_{LS}, the time scale over which the large scale flow changes where, V_{LS} is the large scale velocity. The maximum displacement of the feature was less than one tenth of the tank width so that effects of spatial variations in shear, expected to be substantial only over half the tank width, could be neglected; these measurements could hence be considered local. We make about 11 such measurements of the position of the feature with respect to time at each location. A linear fit between the position and time of the feature is then used to calculate the derivative of the displacement of the feature with time to estimate a single mean velocity V_{sh} along the plume at any location at a given Ra_w and Pr. The errors involved in the estimate of V_{sh} is given in Appendix D.

4.2. *Plume spacing as a function of time*

The merging velocities of plumes at a location were calculated by measuring the position of two merging line plumes at that location from successive images of a merging sequence. The merging pair of line plumes was first identified by viewing a video recording of the time evolution of the whole planform of plume structure. Figure 5(a), and other similar planforms at different Pr, show plumes identified in this way within a dashed ellipse. The co-ordinates of two points- one each on each facing edge of both the plumes in the identified plume pair - that could be connected by a line approximately perpendicular to these line plumes, are captured from mouse clicks by a program. The process is repeated in each successive image of the merging sequence to make about 5 to 20 measurements of pairs of co-ordinates of the merging plumes. The program then calculates the distance between these points in each frame of the merging sequence to obtain the plume spacing λ as a function of time t, the time being calculated from the frame rate of the recording. The maximum error involved in the measurement of λ were of the order of 1%, as estimated from the pixel size of the images. The plume merging period is much smaller than the time scale of the large scale flow and the maximum plume spacing much smaller than the characteristic distance over which the shear is expected to vary spatially so that the measurements would not experience spatial and temporal variations due to variations in the large scale flow; the measurements could be considered local. The slope of a linear curve fit between λ and t then gives us $\lambda' = d\lambda/dt = 2V_m$, where V_m is the locational mean merging velocity at the location at which the measurement is made at any given Ra_w and Pr. The errors involved in the estimate of V_m are discussed in Appendix D.

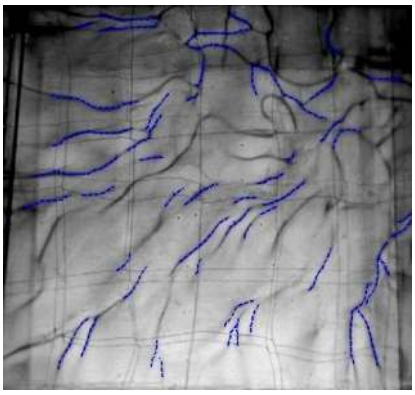

FIGURE 10. Measurement of length of merging plumes (L_{pm}) at $Ra_w = 2.83\times10^7$ and $Pr = 5.08$. The blue (colour online) dashed lines show the parts of the total plume structure that undergo merging

.

4.3. *Merging and sheared plume lengths*

Information on the fraction of the total plume length that is merging at any Ra_w is needed to understand the importance of the merging motion in the total dynamics of the plumes near the plate. We determine this fraction in the following way. A short video clip, of time duration few seconds, is made from the complete video of the time evolution of the planforms. This video clip is played continuously at a much higher speed than the actual recording speed so that merging parts of the plumes could be easily identified. Along with this movie clip, the first planform image from this movie video clip is viewed. Using a program that marks lines on images from mouse clicks and estimates the total length of such lines (Puthenveettil, Gunasegarane, Yogesh, Schmeling, Bosbach & Arakeri 2011) the regions of plumes that are merging in the movie clip are marked with short linear segments in the planform image. Figure 10 shows an example of such a marked planform, where the blue lines are the parts of the plumes that show substantial lateral motion. The program then adds up the total length of the marked lines to give an estimate of L_{pm}, the length of plumes that are merging in the planform at any Ra_w. A similar procedure is also used to estimate L_{ps}, the length of plumes in a planform at a specific Ra_w and Pr that have substantial longitudinal motion along the plumes.

4.4. *Time of initiation of plumes*

We measure t^*, the time of initiation of plumes to understand the physical process by which these plumes are generated. t^* is defined as the time taken for a region in the plume structure to remain vacant of any plume till an initiation occurs as a spot in the vacant region. The initiation of a plume is identified as the first appearance of a spot in an otherwise vacant region in the plume structure. Movies of the evolution of the planforms are repeatedly played while focussing attention in specific regions of the planform so as to spot a location at which a plume is initiated as a point, similar to that shown in figures 8, 9 and 4. Once a location of initiation is identified, the movie is stopped at that frame and the movie is played in reverse while focussing attention on that location.The frame in which the point of initiation first appears and the last frame in which there is no plume at the location of the initiation is noted. The time between these two frames is taken as the time of initiation of a plume t^* at that location. Care is taken not to choose regions where there is substantial plume movement by shear or merging when

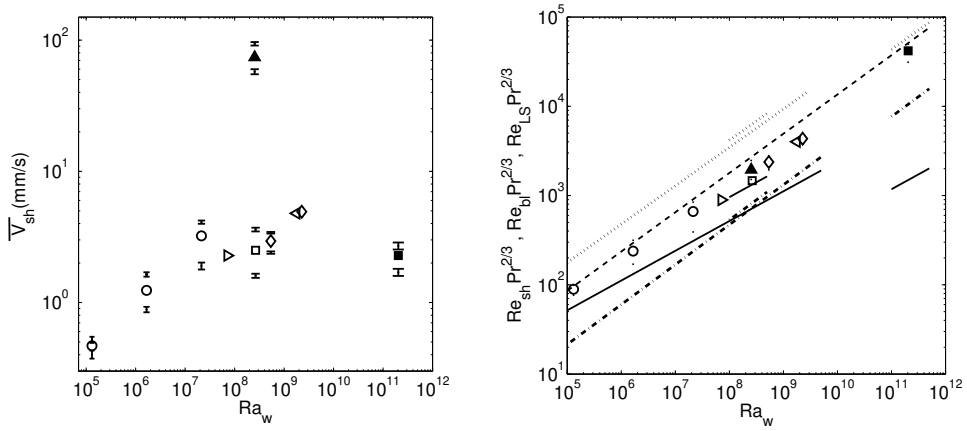

FIGURE 11. (a), Variation of the spatio-temporal mean longitudinal velocity $\overline{V_{sh}}$ with Ra_w for the three Pr. The open symbols show $\overline{V_{sh}}$ for the convection experiments in water for $Pr = 3.6$ to 5.3 for the following layer heights; $\circ$, $H = 50$mm; $\triangleright$, $H = 100$mm; $\square$, $H = 150$mm; $\triangledown$, $H = 200$mm and $\diamond$, $H = 210$mm. $\blacktriangle$ represent experiments at $Pr = 0.74$ and $H = 500$mm while $\blacksquare$ represent experiments at $Sc = 602$ and $H = 230$mm; The vertical range of data shows the range of variation of the locational mean V_{sh}. The error bar indicate the error in V_{sh} at its maximum and minimum values. (b), Variation of Re_{sh}, the Reynolds number based on $\overline{V_{sh}}$ with Ra_w. $- - -$ $Re_{LS} = 0.55Ra_w^{4/9}Pr^{-2/3}$ (Puthenveettil & Arakeri 2005), $\cdots$ $Re_{LS} = 1.47Ra_w^{0.43}Pr^{-0.76}$ (Xia, Lam & Zhou 2002), $- \cdot -$ $Re_{LS} = 0.139Ra_w^{0.447}Pr^{-2/3}$ (Ahlers, Grossman & Lohse 2009) and — $Re_{bl} = 0.19Ra_w^{1/3}Pr^{-0.98}$ (5.2) shown for each of the Pr separately.

these measurements are undertaken. This procedure is repeated at different locations on the planforms for a given Ra_w and Pr and the mean time of initiation of plumes $\overline{t^*}$ is determined from such multiple measurements. There certainly is some amount of subjectivity in these measurements, not in identifying the frame of initiation, but in identifying the frame beyond which the region is not vacant. However by repeating the measurements and taking the mean, the error due to this subjectivity is minimised; the error in t^* is discussed in Appendix D.

5. Dynamics of line plumes

We now quantify the three main dynamics that we described qualitatively in § 3.1, § 3.2 and § 3.3. We focus more on quantifying the dynamics of merging of plumes since far less is known on this type motion compared to the other two.

5.1. *Longitudinal motion of plumes*

Figure 11(a) shows the variation of the spatio-temporal mean velocity of longitudinal motion along the plumes $\overline{V_{sh}}$, at various Ra_w and Pr. $\overline{V_{sh}}$ was calculated as the mean of locational means V_{sh}, measured as discussed in § 4.1, at five locations at various times at a given Ra_w and Pr. We choose the locations to include regions with no alignment and regions with complete alignment so as to approximately span the range of expected longitudinal velocities at any $Ra_w - Pr$ combination. The vertical span of the data in the figure show the range of V_{sh} at some of the Ra_w and Pr. Such variations between locations are not errors, but actual physical variations because of the spatial and temporal

variation of large scale flow strength due to physical reasons mentioned earlier. The error bars show the error in V_{sh} at the maximum and minimum value of V_{sh}, estimated as discussed in Appendix D.

$\overline{V_{sh}}$ increase with increase in Ra_w and decrease in Pr. At the lower Ra_w in water, the velocities are small (~ 0.45mm/s) but become appreciable with increase in Ra_w and is quite substantial at about 16cm/s in air at an Ra_w of 10^8. There also seems to be an approximate trend of increasing range of longitudinal velocities with increasing Ra_w at the same Pr. Since these behaviours are also exhibited by the large scale flow in turbulent convection we expect the longitudinal motion of plumes to be caused by the shear of the large scale flow; we now verify this by comparing $\overline{V_{sh}}$ with the large scale flow velocities in turbulent convection.

Figure 11(b) shows the expressions for the large scale flow strength, in terms of the corresponding Reynolds number $Re_{LS} = V_{LS}H/\nu$, proposed by Puthenveettil & Arakeri (2005), Lam *et al.* (2002) and Grossman & Lohse (2002), along with the variation of $Re_{sh} = \overline{V_{sh}}H/\nu$, the Reynolds number based on the mean longitudinal velocity on the plumes. The first expression is obtained from the observation that the flux, normalised by the diffusive flux in terms of variables near the plate, is a constant for all Ra and Pr and by using this expression of flux in the expression for the characteristic bulk velocity given by Deardorff (1970), see Puthenveettil & Arakeri (2005) for details. The expression by Lam *et al.* (2002) is a curve fit to their experimental data, while that by Grossman & Lohse (2002) is an outcome of the well known scaling theory by the authors which assume Prandtl-Blasius velocity boundary layers near the plate. The magnitude and scaling of Re_{sh} is almost the same as that of Re_{LS} proposed by Puthenveettil & Arakeri (2005),

$$Re_{LS} = 0.55 Ra_w^{4/9} Pr^{-2/3}. \tag{5.1}$$

It would hence be plausible to conclude that the longitudinal motion along the plumes is caused by the shear of the large scale flow on these plumes, since there is no other obvious force, other than that caused by the shear of the large sale flow, that would be needed to balance the viscous resistance against the longitudinal motion along the plumes.

This shear on the plumes also act on the boundary layers in between the plumes so that with increasing Ra_w, the local boundary layers between the plumes will be affected by the external shear of the large scale flow. Such an inference could be formed by comparing the magnitudes of the horizontal velocities inside the local boundary layers feeding the plumes and the large scale flow velocities. Figure 11(b) shows the variation of

$$Re_{bl} = u_{bl}H/\nu = \left(\frac{C_1}{2}\right)^{1/5} Ra_w^{1/3} Pr^{\frac{n_1}{5}-1}, \tag{5.2}$$

the Reynolds number in terms of u_{bl}, the horizontal characteristic velocity inside the natural convection boundary layers feeding the plume from each side at its base, as obtained from (A12) and (A11) of Puthenveettil *et al.* (2011), by using (1.2) and (C 1), where, $C_1 = 47.5$ and $n_1 = 0.1$. Re_{bl} is an order of magnitude smaller than Re_{sh}, the difference in magnitudes between the Reynolds numbers increasing with increasing Ra_w. Hence, at larger Ra_w, the large scale flow will affect the flow inside the local natural convection boundary layers to turn them into mixed convection boundary layers, eventhough the value of external shear given by (5.1) is at a much higher location than the height at which the natural convection boundary layers turn into a plume (see Puthenveettil *et al.* (2011))

Such an effect of the external shear on the natural convection boundary layers could be detected, eventhough qualitatively, from our visualisations. The dashed arrows in fig-

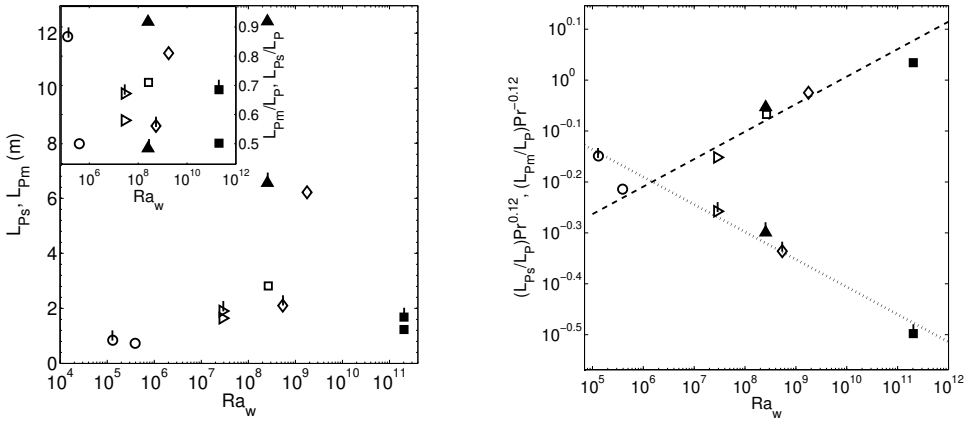

(a) (b)

FIGURE 12. (a) Variation of L_{ps}, the plume length that have longitudinal motion along them and L_{pm}, the plume length that are merging with Ra_w and Pr. The symbols with vertical line indicate L_{pm} while others indicate L_{ps}. The open symbols indicate thermal convection experiments in water for $Pr = 3.6$ to 5.3 for the following layer heights; ○, $H = 50$mm; ▷, $H = 100$mm; □, $H = 150$mm; and ◇, $H = 210$mm. ▲ represents an experiment at $Pr = 0.74$ and $H = 500$mm while ■ represents an experiment at $Sc = 602$ and $H = 230$mm. The inset shows the variation of L_{ps}/L_p and L_{pm}/L_p. (b) The scaling of L_{ps}/L_p and L_{pm}/L_p. The dashed line indicate (5.9) while the dotted line indicate (5.10)

ure 23(a) shows the motion in the boundary layers in between the plumes in a region where there is no substantial shear. The dashed arrows are drawn parallel to the dye streaks seen in the figure; the streaks are formed when the dye layer formed on the plate gets drawn in the predominant motion direction. The motion is approximately perpendicular to the plumes, as would be expected if the boundary layers were natural convection boundary layers feeding the plume at its base. However in figure 9(a), which has more external shear due to the higher Ra_w, the motion in the boundary layers in between the plumes is inclined in the direction of the external shear as shown by the dashed arrows in the figure; we could expect these boundary layers to be of mixed convection nature. At any Ra_w and Pr, there are regions in the planforms with substantial shear along the plumes as well as without it. Hence, the boundary layers feeding the plumes would show a varying nature between pure natural convection type and mixed convection type at various locations, based on the relative magnitude of the external shear and the characteristic velocity of natural convection boundary layers at each location; the former given by (5.1), while the latter by (5.2).

It is hence important to get an idea of the extent of the bottom plate area affected by the external shear at different Ra_w and Pr. One parameter that is indicative of the area affected by shear is L_{ps}, the length of plumes that have noticeable shear along the length of the plumes, measured as discussed in § 4.3. Figure 12(a) shows the variation of L_{ps} for various Ra_w and the three Pr. The length of plumes affected by shear increases sharply with increase in Ra_w and with decrease in Pr, both these changes also increase the strength of the large scale flow as per (5.1). The inset in figure 12(a) shows the variation of L_{ps}/L_p, the fraction of the length of plumes that have noticeable shear along their length, with Ra_w and Pr. L_{ps}/L_p has a weak, positive dependence on Ra_w and a negative dependence on Pr. It is clear from figure 12(a) that along with an increase

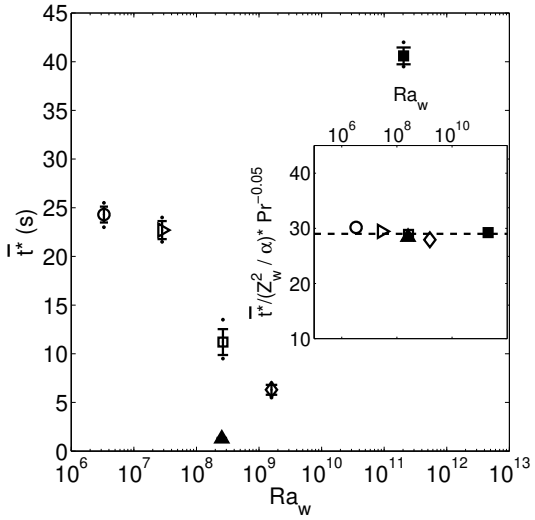

FIGURE 13. Variation of $\overline{t^*}$, the mean time for initiation of plumes as points with Ra_w at the three Pr. The open symbols indicate thermal convection experiments in water for $Pr = 3.6$ to 5.3 for the following layer heights; ○, $H = 50$mm; ▷, $H = 100$mm; □, $H = 150$mm; and ◇, $H = 210$mm. ▲ represents experiments at $Pr = 0.74$ and $H = 500$mm while the ■ represents experiments at $Sc = 602$ and $H = 230$mm. The dots above and below the symbols show the range of time of initiation of plumes (t^*) over the planform for a given Ra_w. The error bars show an estimate of the error in $\overline{t^*}$. The inset shows that the dimensionless time of initiation of plumes is a constant for a given Pr, while the dashed line is (5.6).

in the length of plumes affected by shear, their fraction to the total plume length also increase with increase in large scale flow strength.

A power law fit to L_{ps}/L_p gives us,

$$\frac{L_{ps}}{L_p} = 0.29 Ra_w^{0.058} Pr^{-0.147}. \tag{5.3}$$

Using the expression for L_p from Puthenveettil *et al.* (2011), wherein $L_p \sim Ra_w^{1/3} Pr$, the scaling of (5.3) would imply that

$$L_{ps}/(A/H) = 0.006 Ra_w^{0.39} Pr^{-0.25}, \tag{5.4}$$

a strong positive dependence on Ra_w. Interestingly, in § 5.3.1, we find an approximately similar, but inverse, dependence of that in (5.3) for the fraction of plume lengths that is merging.

5.2. *Initiation of plumes*

It was observed in § 3.3 that plumes usually initiate as points in regions that are free of line plumes, the time for such initiation at a location t^* was measured as discussed in § 4.4. Figure 13 shows the variation of $\overline{t^*}$, the spatio-temporal mean time of initiation of point plumes at various Ra_w and Pr. The mean was calculated from 5 measurements at different locations and times at each $Ra_w - Pr$ combination, the dots above and below the symbol show the range of data from these measurements, while the thick error bar shows the error in $\overline{t^*}$; the details of the error calculations are given in Appendix D.

Plumes initiate faster at larger Ra_w and at lower Pr. As per Howard (1964), initiation of plumes occur by periodic eruption of the boundary layer that grows by a diffusive

process as $\delta(t) = \sqrt{\pi\alpha t}$. The boundary layer erupts at a time t_D at which the Rayleigh number based on the boundary layer thickness $Ra_\delta = g\beta\Delta T_w\delta^3/\nu\alpha$ becomes approximately 1000. Using the value of δ at t_D in the expression for Ra_δ and using (1.2) to rewrite in terms of Z_w, we obtain

$$t_D \sim \frac{100}{\pi}\frac{Z_w^2}{\alpha}, \tag{5.5}$$

with an unspecified Pr dependence, since the stability condition $Ra_\delta \sim 1000$ has an unknown Pr dependence (Puthenveettil, Gunasegarane, Yogesh, Schmeling, Bosbach & Arakeri 2011). As per (5.5), the time of initiation of plumes is proportional to Z_w^2/α, the diffusive time scale near the plate. The inset in figure 13 shows that the measured mean times of initiation of the point plumes scale as

$$\overline{t^*} = 29\frac{Z_w^2}{\alpha}Pr^{0.05}, \tag{5.6}$$

quite close to (5.5).

5.3. *Merging of plumes*

5.3.1. *Fraction of merging length*

As discussed in § 3.2, the complete length of a plume line is not in merging motion at any instant. Some measure which indicate the extent of the merging motion in the planform is hence necessary to decide the importance of merging in the complete dynamics of plumes near the plate.

The length of plumes that are merging in a planform at an instant (L_{pm}), measured as discussed in § 4.3, is an indicator of the spatial extent of the merging dynamics in the overall dynamics near the plate. Figure 12(a) shows the variation of L_{pm} with Ra_w measured at the three Pr. In the thermal experiments with water, up to $Ra_w \sim 10^8$, the extent of merging is slightly more than the extent of longitudinal motion. Almost 90% of the length of the plumes undergoes merging motion at the lowest Ra_w, as seen in the inset of figure 12(a) that shows the variation of the fraction of the length of plumes that display merging motion (L_{pm}/L_p). For $Ra_w > 10^8$ at $Pr \sim 5$, L_{pm} becomes lesser than L_{ps}; the inset shows that L_{pm}/L_p decreases with increase in Ra_w, with L_{pm}/L_p becoming about 55% at $Ra_w \approx 10^9$ in water at $Pr \sim 5$. Similarly, it is clear that L_{pm}/L_p decreases with decrease in Pr by comparing the data of air at $Ra_w \approx 2.5 \times 10^8$ with that of water. It appears that an increase in Ra_w and decrease in Pr results in an increase in shear on the plumes. An increase in shear not only reduces the merging velocities, but also reduces the fraction of plume length that merge, eventhough the total length of plumes that merge still increase with Ra_w.

A power law fit for L_{pm}/L_p gives,

$$\frac{L_{pm}}{L_p} = 1.36Ra_w^{-0.052}Pr^{0.104}. \tag{5.7}$$

Using the expression for L_p from Puthenveettil *et al.* (2011) in (5.7), L_{pm} scales as

$$\frac{L_{pm}}{A/H} = 0.03Ra_w^{0.28}Pr^{0.004}, \tag{5.8}$$

a strong positive dependence on Ra_w, which however is not as strong as that in (5.4). Note that the power law exponents of (5.7) are quite close to, but inverse of, those in (5.4). As shown in figure 12(b), an exact inverse dependence on Ra_w and Pr for L_{pm}/L_p

and L_{ps}/L_p, namely

$$\frac{L_{ps}}{L_p} = 0.29 Ra_w^{0.054} Pr^{-0.12}, \tag{5.9}$$

$$\frac{L_{pm}}{L_p} = 1.36 Ra_w^{-0.054} Pr^{0.12}, \tag{5.10}$$

instead of the expressions (5.4) and (5.7), also fits the data nicely with no change in prefactors from those in (5.3) and (5.7). Such an exact inverse relationship implies that

$$\frac{L_{ps} L_{pm}}{L_p^2} \approx 0.4, \tag{5.11}$$

a dimensionless invariant number for all the fluids in thermal convection. Equation (5.11) is an outcome of the adjusted forms of (5.3) and (5.7), the physical reasons for both of which lie in the complex, not well understood, interaction of the plume structure with the large scale shear. Further investigations of the interaction between shear and plumes need to be done to understand the reason for the relations (5.3), (5.7) and hence (5.11).

The critical Rayleigh number near the plate Ra_{wc}, at which $L_{ps} = L_{pm}$, gives the Rayleigh number below which merging is predominant. By equating (5.9) and (5.10), we get,

$$Ra_{wc} = 1.64 \times 10^6 Pr^{11/5}, \tag{5.12}$$

implying that $L_{pm} > L_{ps}$ for $Ra_w < 8.4 \times 10^5$ at $Pr = 0.74$, for $Ra_w < 5.8 \times 10^7$ at $Pr = 5$ and for $Ra_w < 2.43 \times 10^{12}$ for $Sc = 602$. Clearly, $L_{pm} > L_{ps}$ in our range of Ra_w only for our concentration driven experiments in water at $Sc = 602$. $L_{ps} > L_{pm}$ for all our experiments with air and for half the range of our Ra_w in thermal experiments in water.

5.3.2. *Variation of merging velocities during the merging process*

Figure 14(a) shows the variation of the plume spacing (λ) with time for air, obtained by measurements as described in § 4.2, at the locations shown in figures 2(a) and 5(a) at $Ra_w = 2.54 \times 10^8$. The results of similar measurements corresponding to the locations in figures 3(a) and 6(a) for $Pr = 4.7$ and corresponding to figures 4(a) and 7(a) for $Sc = 602$ are shown in figures 14(b) and 14(c) respectively. As is obvious from figures 14(a) to 14(c), variations of λ with t are strong functions of Ra_w and Pr. More importantly, the variation of λ in all these plots is approximately linear with time. Such linear behaviour of λ with t were obtained for all the measurements at different Ra_w for all the three Pr at all the locations of a planform. The maximum variation of the data from linearity was of the order of 5% from all the curve fits. Due to such a linear variation of λ with time at all Ra_w and Pr, we estimate the merging velocities of plumes by calculating the gradient of a linear curve fit through the measured λ vs t. A linear variation of λ with t would imply that the plumes merge with a constant locational mean velocity, $V_m = \lambda'/2$ where $\lambda' = d\lambda/dt$, during their merging period, eventhough the value of this constant velocity is itself different at different locations at the same Ra_w, as shown by figure 14. Appendix C shows that appreciable merging velocity is detected in our measurements only when plumes come close to a distance of the order of $\overline{\lambda}$. However, the constant V_m during a merging cycle is unlikely to be due to the short distance over which the merging is measured since, as we show in § 6.2, there is a strong physical reason for it to be so.

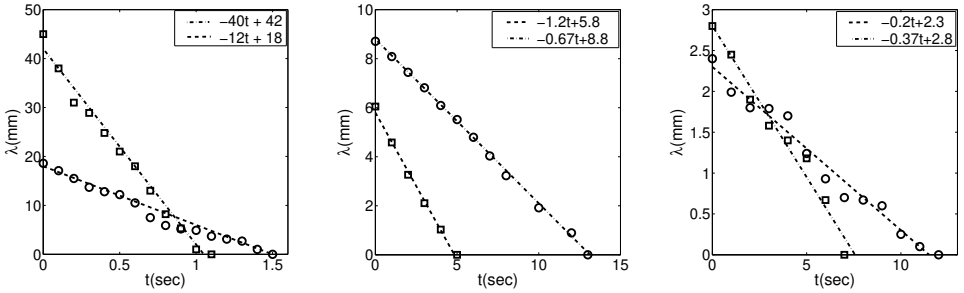

FIGURE 14. Measured variation of plume spacings (λ) as a function of time (t) in regions with shear ($\circ$) and without shear ($\square$) for; (a), $Pr = 0.74$ at $Ra_w = 2.54 \times 10^8$; (b), $Pr = 4.7$ at $Ra_w = 2.65 \times 10^8$ and; (c), $Sc = 602$ at $Ra_w = 2.034 \times 10^{11}$.

5.3.3. *Statistics of merging velocities*

Figure 14 showed that plumes in low shear regions merged faster than those in the shear dominated regions. Since the shear due to the large scale flow is a function of space (Puthenveettil & Arakeri 2005; Qiu & Xia 1998), at any instant, the instantaneous merging velocities (V_{mi}) in a planform are distributed over a range of values. On the other hand, at any location, for a given Ra_w and Pr, the V_{mi} in different merging sequences could also be a function of time since the shear at that location is also not constant due to the azimuthal rotations and reversals of the large scale flow (Ahlers *et al.* (2009)). Hence, at any Ra_w and Pr, V_{mi} are functions of space and time.

We estimate this distribution of V_{mi} at any Ra_w and Pr by measuring the merging velocities from various merging sequences at different locations and times for that Ra_w and Pr. At each Ra_w, about 30 plume merging sequences on the planforms were identified at different times from regions with and without shear. From these sequences, a total of about 280 plume merging velocities were measured. Since these are instantaneous velocities and not locational mean over time, V_{mi} during any merging sequence were calculated by estimating $d\lambda_i/dt$ from successive values of the instantaneous plume spacing, λ_i in time, and not from a curve fit as in § 4.2.

Figure 15 shows the probability density function (pdf) of V_{mi} obtained from these measurements at four different Ra_w for the three Pr. Comparing the $Pr = 4.7$ and 0.74 curves in the figure ($\square$ and ▲), which are approximately at the same Ra_w, it is clear that a decrease in Pr results in a higher spatio-temporal mean merging velocity $\overline{V_m}$ where, $\overline{V_m}$ is the mean of V_{mi}. Plumes merged faster at a lower Pr at the same Ra_w. Since viscous effects will be lower in a lower Pr fluid, the resistance to merging motion will be lower, the mean merging velocities could hence be expected to be larger. However, lower Pr also results in larger shear velocities due to the stronger large scale flow (Ahlers, Grossman & Lohse 2009); as we saw earlier, this shear slows down the merging. Such slowing of merging due to the increase in the strength of the large scale flow do not seem to be the dominating effect compared to the possible increase in merging velocities due to the reduction in viscous resistance to merging. The range of V_{mi} observed at a smaller Pr was larger than that at a higher Pr, as could be noticed from the spread of the pdfs $\square$ and ▲ in figure 15. The higher shear at the lower Pr could again be the reason for such a behaviour of the pdfs. The shear at smaller Pr would have larger variations across the planform since it has to be negligible near the side walls while its value at the centre will increase obeying the standard relations for the large scale flow strength(Ahlers, Grossman

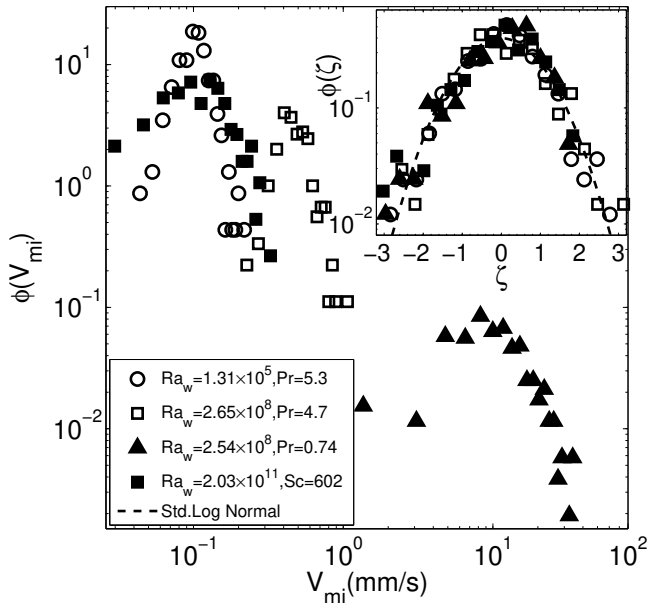

FIGURE 15. Distribution of the instantaneous merging velocity of plumes (V_{mi}) for different Ra_w and Pr. The inset shows the data in the main figure plotted as the pdf of the logarithm of the dimensionless merging velocities in their standardised form $\zeta = (\ln(V_{mi}/\overline{V_m}) - \overline{\ln(V_{mi}/\overline{V_m})})/\sigma \ln(V_{mi}/\overline{V_m})$.

& Lohse 2009); similar would be the corresponding variation of V_{mi} since shear reduces V_{mi}.

Comparing the pdfs at $Ra_w = 1.31 \times 10^5$ and 2.65×10^8, which are approximately at the same Pr ($\circ$ and $\square$ in figure 15) it could be noticed that the mean merging velocity increased with increase in Ra_w. Plumes merge faster with increase in Ra_w at the same Pr, presumably since more amount of heat has to be transported into the bulk at a larger Ra_w. The range of merging velocities also increase with increase in Ra_w, since the range of variation of shear on the planform increases with Ra_w due to the same reason for the larger range of V_m with lower Pr. The pdf for $Ra_w = 2.03 \times 10^{11}$ and $Sc = 602$ show the combined result of the opposing effects of increase in Ra_w and Sc. For this data, the effect of an increase in Sc seems to be dominant than an increase in Ra_w since the mean and the range of V_m are lower than those obtained at lower Ra_w.

The noticeable common trend from all the curves in figure 15 is that an increase in $\overline{V_m}$ decreases the probability of finding this $\overline{V_m}$ in any planform; the curves are shifted downward with increasing values of $\overline{V_m}$ for any fluid. This trend is seen whether the increase in $\overline{V_m}$ occurs due to a decrease of Pr or due to an increase of Ra_w. We expect the reason for this behaviour to be as follows. The total length of plumes in the planform L_p increases as $Ra_w^{1/3}$ and $Pr^{-0.1}$ (Puthenveettil, Gunasegarane, Yogesh, Schmeling, Bosbach & Arakeri 2011). Since $\overline{V_m}$ increases with an increase in Ra_w or a decrease of Pr, an increase in $\overline{V_m}$ will also be accompanied by a larger L_p in the planform. When L_p increases, we expect the total number of merging occurrences, as well as the number of mergings with a specific V_{mi} also to increase. But since this increased number of mergings occur over a larger range of V_{mi}, as we saw earlier, the probability of finding any $\overline{V_m}$ decreases with an increase in $\overline{V_m}$.

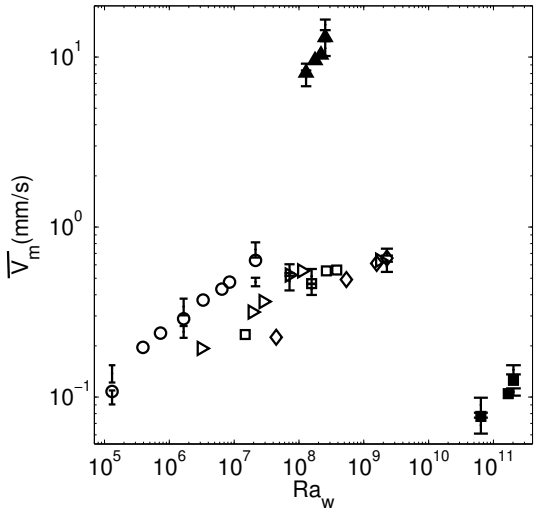

FIGURE 16. Variation of the spatio-temporal mean merging velocity $\overline{V_m}$ with Ra_w for the various Pr. The open symbols show $\overline{V_m}$ for the thermal convection experiments in water at $Pr = 3.6$ to 5.3 for the following layer heights; $\circ$, $H = 50$mm; $\triangleright$, $H = 100$mm; $\square$, $H = 150$mm; $\bigtriangledown$, $H = 200$mm and $\diamond$, $H = 210$mm. The variation of $\overline{V_m}$ for $Pr = 0.74$ at $H = 500$mm is shown by $\blacktriangle$ and for $Sc = 602$ at $H = 230$mm by $\blacksquare$. The vertical range of data show the range of V_m, the locational means at each Ra_w while the error bars show the error in V_m at its maximum and minimum

The inset in figure 15 shows the data in the main figure plotted as the pdf of the logarithm of the dimensionless merging velocities $(V_{mi}/\overline{V_m})$ in its standardised form $\zeta = (\ln(V_{mi}/\overline{V_m}) - \overline{\ln(V_{mi}/\overline{V_m})})/\sigma \ln(V_{mi}/\overline{V_m})$, where, — indicates the mean and σ indicates the standard deviation. All the curves in figure 15 collapse on to the standard log-normal curve, shown as the dashed line. Even though the mean and the variance of V_{mi} increased with increasing Ra_w and decreasing Pr, the probability distribution function has a common log-normal form for all the Ra_w and Pr, the details of which are discussed in Appendix E.

5.3.4. *Mean merging velocities*

Figure(16) shows the variation of $\overline{V_m}$, the spatio-temporal mean velocity of merging of plumes, with Ra_w for the three Pr; the corresponding values are listed in table 1. At each Ra_w, $\overline{V_m}$ was determined as the mean of 5 to 30 values of the locational means V_m measured at different locations at different times. We chose regions with no alignment of plumes to regions with substantial alignment to cover the possible range of V_m at any $Ra_w - Pr$ combination; statistical significance issues becomes less important in such visually guided choice. The vertical span of the data shown at some of the Ra_w show the range of variation of the V_m obtained from such measurements. These ranges do not indicate errors, but show the extent of variation of V_m over the planform at different times that occurs due to physical reasons. The error bars in the figure show the random errors in V_m, located at the maximum and minimum value of V_m; the details of this error estimation are shown in Appendix D.

At all Pr, for any constant H, $\overline{V_m}$ increased with increase in Ra_w; plumes merged faster with increase in driving potential ΔT_w. Variation of $\overline{V_m}$ for thermal convection experiments in water at approximately the same Pr, shown by any of the symbols $\circ, \triangleright, \square$

and $\diamond$ in figure 16, were obtained by changing the heat flux for any constant H. It is clear that a change in layer height results in a horizontal shift of the curve of $\overline{V_m}$ without changing the values of $\overline{V_m}$; as we show later, $\overline{V_m}$ is independent of layer height if the effect of external shear is small. The shift in $\overline{V_m}$ vs Ra_w with H in figure 16 comes only due to the plotting of $\overline{V_m}$ as a function of Ra_w by which the value of Ra_w at the same driving potential is shifted by a fixed value between experiments with different layer heights. Comparing the water and air data at $Ra_w \sim 2.5 \times 10^8$ it could be noticed that the plumes merged much faster at $Pr = 0.74$ than at $Pr = 5.3$. $\overline{V_m}$ is inversely proportional to Pr, as was also observed in figure 15. By comparing figures 16 and 11(a), we also notice that $\overline{V_m}$ are an order lower than $\overline{V_{sh}}$.

6. Scaling of mean merging velocities

We now quantify the observations about $\overline{V_m}$ in § 5.3.4 by building a scaling analysis based on the following assumed phenomenology of merging laminar sheet plumes. Two parallel line plumes that merge, as shown in figure 17(a), originate from the instability of laminar natural convection boundary layers (Pera & Gebhart 1973) that occur on both sides of each plume at its base, (Puthenveettil & Arakeri 2005; Puthenveettil *et al.* 2011). Since these plumes are the outcome of an instability, we expect these plumes to retain their laminar nature till some height. The rising plumes entrain fluid from the ambient through their sides so that the mass flux at any cross section, the velocities inside the plumes and the width of the plumes increase with height (Gebhart, Pera & Schorr 1970). The entrainment flow at the side of the plume at any height is determined by the velocity inside the plumes, which again is determined by the heat flux. For a given heat flux and spacing between the plumes, the flow from the bulk region may not be enough to meet this entrainment flow into the plume; the plumes could then be expected to adjust their horizontal position so that mass and momentum balance of the region between the plumes is maintained. We formalise this phenomenology below by using the unsteady mass and momentum balance of a deforming control volume (CV) in between the plumes.

6.1. *Control volume mass and momentum balance*

As shown in figure 17(b) we choose the width of the CV to be equal to the spacing between the plumes $\lambda(t)$ which is a function of time t. The height h of the CV is chosen as the height to which the diffusive region near the plate extends upwards. $h = aZ_w$, the position at which the mean profiles of temperature, velocity and their fluctuations do not show substantial variation with height (see Theerthan & Arakeri (2000, 1998)). Here, for the time being, a is assumed to be a constant and Z_w is the length scale defined by (1.2). In actuality, a is a function of Pr; we will see later that this has to be so for our theory to exactly match the experiments in its Pr dependence. $a \approx 40$ for $Pr \sim 1$ so that for the usual range of Ra_w, $h < 1$ cm. Over this small height, at a scaling level, one could neglect the variation of the plume thickness with height in estimating the volume of fluid in between the plumes. Further since $\delta_v \ll h$, we neglect the contribution of the boundary layers on the plate in estimating the volume of the fluid in between the plumes. Under these assumptions, the mass balance becomes,

$$2\rho_b h V_m \approx \rho_b V_b \lambda - 2\rho_b \int_0^h V_h dy, \tag{6.1}$$

where, as shown in figure 17(b), ρ_b is the density of the bulk fluid, $V_b(t)$ the downward velocity of the bulk fluid at the top surface of the CV and $V_h(y)$ the horizontal entrain-

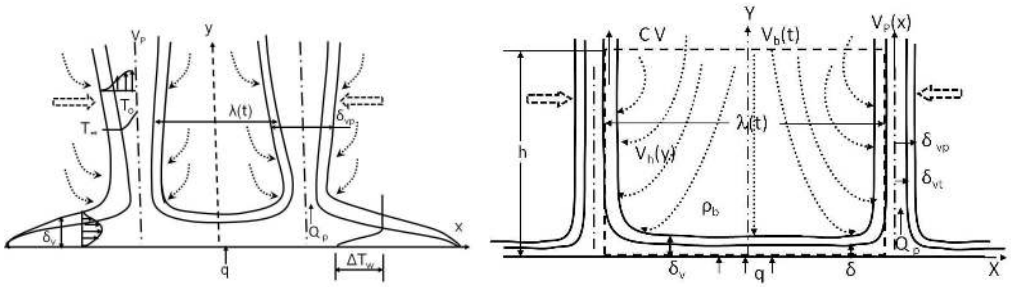

FIGURE 17. (a), Schematic of two adjacent line plumes on the plate that are merging at any instant, separated by the plume spacing $\lambda(t)$. The hollow arrows show the direction of merging and the curved arrows the entrainment into the plumes. (b), The idealisation used for the scaling analysis of $\overline{V_m}$. The deforming control volume (CV) of height of h and width $\lambda(t)$ is shown as the dashed line. $V_b(t)$ is the uniform velocity of the bulk fluid into the CV at the top surface of the CV at any instant, $V_h(y)$ is the velocity of the fluid entrained into the plume at the edge of the plume, $V_p(x)$ is the velocity distribution inside the plume at a height of h. The thickness of the velocity boundary layer feeding either side of a plume is δ_v while the plume velocity boundary layer thickness is δ_{vp}. q is the total heat flux supplied to the plate and Q_p is amount of heat transported by the plume per unit length at any height.

ment velocity at the edge of the plumes at any height y. Equation (6.1) shows that the rate of change of mass of the bulk fluid in between the plumes due to the merging of the plumes is equal to the difference between the influx from the bulk and the out flux due to the entrainment by the plumes. Since $V_h(y)$ could be obtained as a function of Ra_w and Pr from the similarity solutions of Gebhart *et al.* (1970), (6.1) could be used to obtain the scaling of V_m, if V_b is known, or could be eliminated by another equation. The momentum balance of the fluid in between the plumes gives us such an equation.

By vertical momentum balance in the CV, we get,

$$\frac{\partial}{\partial t}\left(\rho_b \lambda \int_{\delta_v}^{h} V dy\right) \approx \rho_b g h \lambda - \Delta P \lambda + \rho_b V_b^2 \lambda, \tag{6.2}$$

under the same assumptions used in obtaining (6.1). Here, $V(y)$ is the vertical velocity distribution in between the plumes and ΔP the pressure difference between the bottom and the top of the CV. The pressure drop across the boundary layer on the plate ($\sim g\Delta\rho\delta_T$, see § A.2 in Puthenveettil *et al.* (2011)) is neglected in comparison to the pressure drop in the rest of the height of the CV, $\rho_b g(h - \delta_T)$. The above equation shows that the rate of change of vertical momentum in between the plumes will be equal to the sum of the net vertical force and the influx of vertical momentum due to the inflow of bulk fluid at the top of the CV. We now estimate the unknown ΔP in (6.2) using unsteady Bernoulli equation.

The flow in between the plumes could be assumed to be irrotational, except in the boundary layer region, as was shown by Schneider (1981) for the case of axisymmetric plumes. We neglect the pressure drop across the boundary layers on the plate and the entrainment velocity at the edge of the boundary layers on the plate in comparison to the velocity at the top of the CV, and assume that $h - \delta_v \approx h$. Then, by applying unsteady Bernoulli equation between the top of the CV and at the edge of the boundary layer, we obtain,

$$\Delta P \approx \frac{1}{2}\rho_b V_b^2 + \rho_b g h - \rho_b \frac{\partial}{\partial t}\int_{\delta_v}^{h} V dy. \tag{6.3}$$

With the above three equations (6.1), (6.2) and (6.3) we now relate the unknown merging velocity V_m to the entrainment velocity V_h, which could be estimated from the similarity solutions of Gebhart *et al.* (1970).

6.2. *Relationships of merging velocity to velocities of entrainment and plume rise*

Expanding the first term in (6.2) and substituting ΔP from (6.3) in (6.2), we obtain,

$$\frac{V_b \lambda}{h} \approx 4 V_m \left[\frac{\int_{\delta_v}^{h} V dy}{V_b h} \right] \sim 4 V_m, \tag{6.4}$$

since $\int_{\delta_v}^{h} V dy$ scales as $V_b h$. Now, the unknown V_b in (6.1) could be eliminated by substituting (6.4) in (6.1) to obtain,

$$V_m \sim \frac{1}{h} \int_0^h V_h dy. \tag{6.5}$$

In other words, the lateral merging velocity of the plumes V_m is equal to the average entrainment velocity at the sides of the plumes where, the averaging is done over the height of the diffusive zone near the plate.

We could also relate the merging velocity of plumes to their rise velocity as follows. By mass balance of the plume,

$$2 \int_0^h V_h dy = \int_{-\delta_{vp}}^{\delta_{vp}} V_p dx, \tag{6.6}$$

where $V_p(x)$ is the velocity distribution inside the plume across the thickness of the plume of $2\delta_{vp}$ at a height of h. Equations (6.5) and (6.6) would then imply that

$$V_m \sim \overline{V_p} \, \frac{\delta_{vp}}{h}, \tag{6.7}$$

where $\overline{V_p}$ is the average plume rise velocity at a height of h. Since $\delta_{vp} \ll h$, equation (6.7) implies that the merging velocities of the plumes are an order lower than the plume rise velocities. Since the velocity of large scale circulation also scales as the velocity of rise of plumes (Puthenveettil & Arakeri 2005), the merging velocities of the plumes would be an order lower than the large scale circulation velocity as was observed in figures 16 and 11(a). We observed in § 5.3.2 that the merging velocities are constant during any merging sequence at a fixed Ra_w. It is easy to understand the cause for this behaviour from (6.5) and (6.7). At any Ra_w, the strength of two adjacent plumes could be expected to be constant over their merging period. This would imply from (6.6) that their average entrainment velocity also remains constant during the merging cycle; (6.5) would then imply that the merging velocities are also constant.

6.3. *The entrainment flow into the plumes*

We have seen in (6.5) that the velocity of merging of plumes is related to $\int_0^h V_h dy$, the total entrainment flow into the plume through one of its sides, over the height of the diffusive region near the plate. We now need to estimate this entrainment flow as a function of Ra_w and Pr to find the scaling of merging velocities. As given by Gebhart *et al.* (1970), the velocity of entrainment at the edge of a two dimensional plume above a heated line source at any height y is

$$V_h(y) = \frac{3 \times 4^{3/4}}{5} \frac{\nu}{y} Gr_y^{1/4} f(\eta_{\delta_{vp}}), \tag{6.8}$$

where, $\eta_{\delta_{vp}}$ is the value of the similarity variable $\eta = (Gr_y/4)^{1/4}x/y$ of Gebhart *et al.* (1970) at the velocity boundary layer thickness δ_{vp}. $f(\eta)$ is the dimensionless stream function defined by $\psi = 4\nu(Gr_y/4)^{1/4}f(\eta)$, with the local Grashoff number,

$$Gr_y = g\beta(T_0 - T_\infty)y^3/\nu^2. \tag{6.9}$$

$f(\eta_{\delta_{vp}}) = a_1 Pr^{-b_1}$ where $b_1 = 0.4$ for $Pr < 1$ and 0.2 for $Pr > 1$, while $a_1 = 0.8$ for all Pr as obtained from Gebhart *et al.* (1970). Here, $T_0 - T_\infty$ is the temperature difference between the center line of the plume and the ambient, which decreases with y as follows

$$T_0 - T_\infty = \left(\frac{Q_p}{\rho C_p I}\right)^{4/5}\left[\frac{1}{4^3 g\beta\nu^2 y^3}\right]^{1/5}, \tag{6.10}$$

where $I = 1/\sqrt{Pr}$ from Gebhart *et al.* (1970), C_p is the specific heat at constant pressure and Q_p is the heat flux into each line plume. As shown in Appendix F,

$$Q_p = (C_2 Pr^{n_2})^4 \frac{\rho C_p}{g\beta}\left(\frac{\alpha}{\overline{\lambda}}\right)^3, \tag{6.11}$$

as obtained by relating Q_p to q by heat balance and then using the expression (F 5) for $\overline{\lambda}$ in terms of Z_o, the Townsends near-wall length scale (F 4).

We now substitute (6.11) in (6.10) and use the resulting expression for $T_0 - T_\infty$ in (6.9) to obtain the expression for local Gr_y. Using this expression for Gr_y in (6.8), we integrate the resulting expression for V_h with respect to y from 0 to $h = aZ_w$. Replacing $\overline{\lambda}$ in the resulting expression with (C 1) we obtain,

$$\int_0^h V_h\, dy \sim A_1 Pr^B \nu \tag{6.12}$$

where $A_1 = \left(2^6 C_2^4 a^3/C_1^3\right)^{1/5} a_1 = 26$ and $B = (4n_2 - 3n_1)/5 - b_1 - 1/2 = -0.7$ for $Pr < 1$ and $B = -0.5$ for $Pr > 1$. Surprisingly, the total entrainment flow per unit length of line plumes through the sides of the plumes over the height of the diffusive region near the plate, given by (6.12), is independent of Ra_w and is only a function of viscosity and Pr, when the line plumes are separated by a mean spacing of $\overline{\lambda}$.

6.4. *Scaling of λ'*

Substituting (6.12) in (6.5), we obtain,

$$\overline{V_m} = APr^B \frac{\nu}{Z_w}, \tag{6.13}$$

where $\overline{V_m}$ is the spatio-temporal mean merging velocity and $A = A_1/a = 0.65$. We use $\overline{V_m}$ instead of V_m in (6.13) since (F 3) is valid for a uniform array of plumes separated by $\overline{\lambda}$. Equation (6.13) shows that the spatio-temporal mean lateral merging velocity of line plumes scales as the velocity scale near the plate ν/Z_w. Note that (6.13) shows that the merging velocity is only a function of the variables near the plate. This is however so because we have neglected the effect of shear in the scaling analysis. As we have seen earlier in § 5.3.2 and § 3.2, shear due to the large scale flow reduces the merging velocity of plumes; if the effect of shear is not substantial, the above scaling is expected to hold. The Pr dependence of $\overline{V_m}$ shown in figure 16, where higher Pr fluids had lower merging velocities seems to be captured by the Pr dependence in (6.13). The horizontal shift in V_m, observed in figure 16, between experiments with different heights of fluid layer at the same Pr could also be understood from (6.13). Since V_m is not a function of H, at least to first order, change in H in the Ra_w in the abscissa of the plot will shift the data

without changing its scaling. We now quantitatively compare the scaling law of (6.13) with the experimental data of figure 16 in three different dimensionless forms.

6.4.1. *Reynolds number relation*

The scaling law of (6.13) could be rewritten as a Reynolds number as,

$$Re_H = \overline{V_m}H/\nu = ARa_w^{1/3}Pr^B. \tag{6.14}$$

As shown in figure 18, the measured mean merging velocities, in terms of Re_H, scale as,

$$Re_H = 0.55Ra_w^{1/3}Pr^{-3/4}, \tag{6.15}$$

at all Pr. The Ra_w dependence in the theoretical scaling of Re_H (6.14) matches exactly with the experiments for all Pr; the difference in the prefactor between theory and experiments is also small (0.65 as against 0.55). Same is the case with the exponent of Pr (-0.7 as against -0.75) for experiments with $Pr < 1$. These agreements are remarkable considering the approximations that were made in the theory and the presence of spatially varying shear in experiments which is not considered in the theory. Equation (6.14) and (6.15) imply that $\overline{V_m}$, normalised by the viscous velocity scale ν/H, scales as $Ra_w^{1/3}$ for a given fluid. Such a scaling is similar to the scaling of the dimensionless plume length $L_P/(A/H)$ and Nu in turbulent convection, in the usually encountered case of low or negligible shear by the large scale flow on the natural convection boundary layers. The dependence of Re_{bl} (5.2), is also shown in figure 18; $Re_{bl} \gg Re_H$, except for $Sc = 602$ where it is slightly less than Re_H. Since the velocities inside the boundary layers feeding the plumes are larger than or close to the merging velocities, the plumes are not detached from these boundary layers during their merging period.

Figure 18 also shows the magnitude and scaling of Re_{LS} (5.1) in comparison with that of Re_H. As shown in figure 11(b), Re_{sh} has the same magnitude and scaling as Re_{LS}. Figure 18 shows that at all Pr, the magnitude of $\overline{V_m}$ is an order of magnitude lower than that of $\overline{V_{sh}}$. The magnitudes of the mean velocities obtained by Hogg & Ahlers (2013) by spatial correlation of images of plumes were substantially lower than that of the large scale velocity. Since we find that mean merging velocities are much smaller than the shear velocities, the mean velocities detected by Hogg & Ahlers (2013) could be the mean merging velocities, which could possibly be interpreted as following the scaling of large scale flow over a smaller range of $10^5 < Ra_w < 10^7$ of Hogg & Ahlers (2013).

For $Pr > 1$, eventhough the theoretical scaling has the same prefactor and dependance on Ra_w as in the $Pr < 1$ case, it has an exponent of Pr equal to -0.5 as against the experimental exponent of -0.75. We now explore the possible cause of this discrepancy between the theory and experiments for $Pr > 1$. The theoretical scaling law (6.14) was obtained by assuming $h = aZ_w = aH/Ra_w^{1/3}$, where $a \approx 40$. However, this relation for the height of the diffusive region near the plate is valid mostly for $Pr \sim 1$ since Pr dependence is not included in the length scale Z_w (see Puthenveettil *et al.* (2011) where the boundary layer thickness is a function of Z_w and Pr). It is hence not surprising that the Pr dependence of the theory is correct for $Pr < 1$, since these experiments are at $Pr \approx 0.74$, close to one. Since our $Pr \gg 1$ experiments are at $Sc = 602$, much larger than one, the Pr dependence in h should be accounted in the theory if a better agreement with experiments is to be achieved at these Pr. However, the Pr dependence of the height of the diffusive region near the plate is not known clearly as of now to get a better match of the theory with the experiments.

It is easy to see that the availability of the above missing information could result in an exact match of the theory with the experiments. We notice that if the height of the

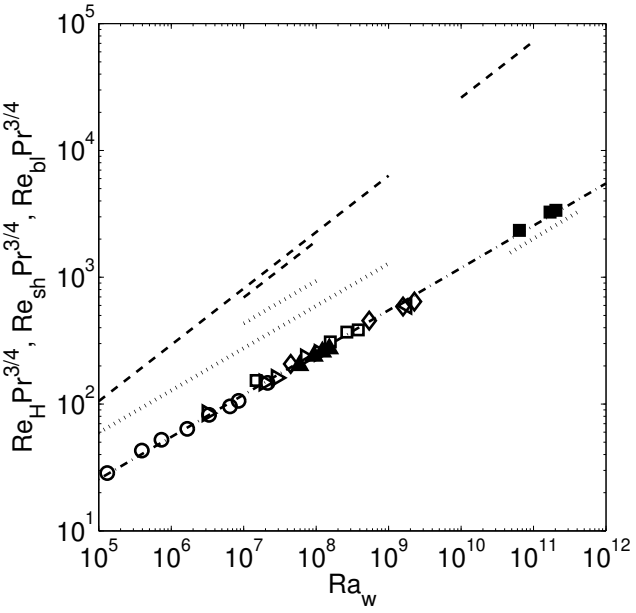

FIGURE 18. Variation of $Re_H = \overline{V_m} H/\nu$, the Reynolds number based on $\overline{V_m}$ and H, with Ra_w. The open symbols indicate thermal convection experiments in water at $Pr = 3.6$ to 5.3 for the following layer heights; $\circ$, $H = 50$mm; $\triangleright$, $H = 100$mm; $\square$, $H = 150$mm; $\triangledown$, $H = 200$mm and $\diamond$, $H = 210$mm. $\blacktriangle$ represent experiments at $Pr = 0.74$ and $H = 500$mm while $\blacksquare$ represent experiments at $Sc = 602$ and $H = 230$mm. $- \cdot - \cdot$ $Re_H = 0.55 Ra_w^{1/3} Pr^{-3/4}$ (6.15); $- - -$, $Re_{LS} = 0.55 Ra_w^{4/9} Pr^{-2/3}$ (5.1) and $\cdots$, $Re_{bl} = 1.9 Ra_w^{1/3} Pr^{-0.98}$ (5.2) plotted for each of the Pr separately.

diffusive region near the plate is a function of Pr so that,

$$a = 60 Pr^{1/8} \text{ for } Pr < 1 \text{ and} \tag{6.16}$$

$$= 60 Pr^{5/8} \text{ for } Pr > 1, \tag{6.17}$$

the theoretical scaling will match the experiments for all Pr. Qualitatively, (6.16) and (6.17) seems to be correct since, as judged from the distributions of mean quantities, the height of the diffusive region near the plate increases with increase in Pr at the same Ra_w (Theerthan & Arakeri 1998).

Due to the above mentioned unavailability of information to make the scaling analysis more rigorous, we assume that the experimental scaling given by (6.15) to be the more reliable one from among (6.14) and (6.15). Alternatively one could assume that the height of the diffusive region near the plate follows the relation $h = aZ_w$, where a is given by (6.16) and (6.17), so that the scaling (6.15) obtained from the experiments match the theory. In addition, in obtaining the scaling shown by (6.4), we had assumed that $\int_{\delta_v}^{h} V dy$ scales as $V_b h$. Such a scaling is mostly correct only at $Pr \leqslant 1$ since viscosity could create vertical variations of vertical velocity in between the plumes at larger Pr. Further research needs to be conducted to verify the assumed Pr depends of the height of the diffusive region near the plate and on the velocity field between the plumes. We now look at the implications of (6.15), interms of the invariants that come out of such a scaling, as well as relate Nu to Re_H.

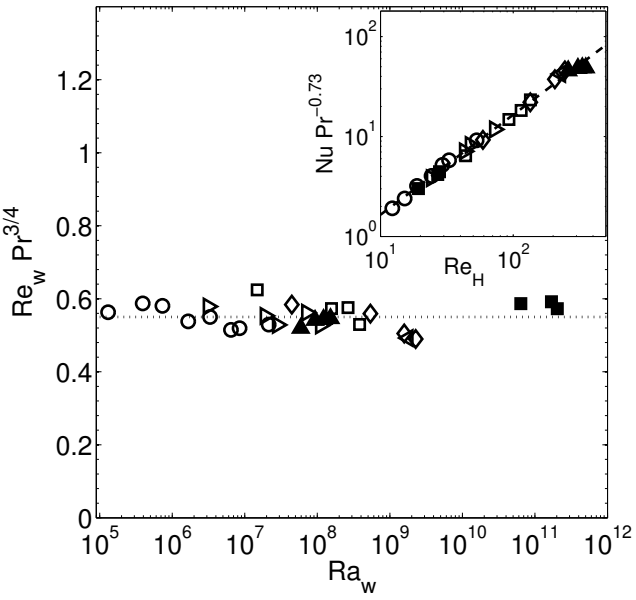

FIGURE 19. Variation of $Re_w = \overline{V_m} Z_w/\nu$, the Reynolds number based on variables near the plate, with Ra_w. The open symbols show experiments in water for $Pr = 3.6$ to 5.3 for the following layer heights; ○, $H = 50$mm; ▷, $H = 100$mm; □, $H = 150$mm; ▽, $H = 200$mm and ◇, $H = 210$mm. ▲ indicate experiments at $Pr = 0.74$ and $H = 500$mm while ■ show experiments at $Sc = 602$ and $H = 230$mm. $\cdots$, $Re_w Pr^{3/4} = 0.55$ (6.18).The inset shows the variation of Nusselt number Nu with Re_H, the Reynolds number based on V_m and layer height H; $---$, $Nu = 0.165 Re_h Pr^{0.73}$ (6.23).

6.4.2. *Invariants*

Equation (6.13) could be rewritten as an expression for a Reynolds number based on the variables near the plate $Re_w = \overline{V_m} Z_w/\nu = 0.55 Pr^{-3/4}$. In other words,

$$Re_w Pr^{3/4} = 0.55 \tag{6.18}$$

is a dimensionless invariant for all the fluids in turbulent convection. Figure 19 shows that (6.18) holds reasonably well for $0.74 \leqslant Pr \leqslant 5.3$ and $Sc = 602$ for $1.31 \times 10^5 \leqslant Ra_w \leqslant 2 \times 10^{11}$ in our experiments. Equation (6.18) means that, the mean merging velocity of the plumes normalised by the velocity scale near the plate ν/Z_w is only a function of Pr, and hence remains an invariant for any given fluid in turbulent convection. If we define a Froude number $Fr_w = \overline{V_m}/\sqrt{g Z_w}$ in terms of the mean merging velocity and the length scale Z_w near the plate, then,

$$Re_w^2 Pr = \frac{Fr_w^2}{\beta \Delta T_w}. \tag{6.19}$$

Using (6.19) and (6.18) we obtain that,

$$\frac{Fr_w^2}{\beta \Delta T_w \sqrt{Pr}} = 0.3 \tag{6.20}$$

is another dimensionless invariant for the dynamics of plumes near the plate in turbulent convection.

6.4.3. *Nusselt number relation*

$\overline{\lambda}$ given by (C 1) is also equal to that given by (F 5), thereby implying that,

$$Z_w = \frac{C_2}{C_1} Pr^{n_2 - n_1} Z_o, \tag{6.21}$$

where Z_o is given by (F 4). We replace the heat flux that appears in Z_o in (6.21) in terms of the Nusselt number $Nu = q/(k\Delta T/H)$. Substituting the resultant expression for Z_w in (6.18), we obtain

$$Re_H = \frac{C_1}{2C_2} Pr^{1+n_1-n_2} (NuRa)^{1/4}. \tag{6.22}$$

Replacing Ra in (6.22) by the expression for Ra obtained from (6.15), we obtain,

$$Nu = 0.165 Re_H Pr^{0.73}. \tag{6.23}$$

The inset of figure 19 shows that the experimental Nu and Re_H obey the above expression satisfactorily. Re_H is directly proportional to the Nusselt number, which should also be obvious from (6.15) since $Nu \sim Ra^{1/3}$ in turbulent convection approximately.

In our $Ra_w - Pr$ range, the exponent in $Nu \sim Ra$ scaling is not exactly 1/3, but very close to it. The exponent is around 0.327, instead of 0.33, in

$$Nu = 0.0714 Ra^{0.327}, \tag{6.24}$$

as given by Ahlers *et al.* (2009) for $Pr = 0.7$. If (6.23) is derived using (6.24) from (6.15), we obtain

$$Nu = 0.161 Re_H^{0.98} Pr^{0.74}, \tag{6.25}$$

for $Pr = 0.7$, a very small change in the $Nu \sim Re_H$ scaling law given by (6.23).

It should be noted that (6.23) has been obtained here by not using any assumed flux scaling relation in turbulent convection. We have only used the relation (F 5) for the mean plume spacing, which could be obtained by the phenomenology of laminar natural convection boundary layers becoming unstable at a critical thickness, as was shown by Puthenveettil *et al.* (2011). Clearly, since the stability condition $Ra_\delta \sim 1000$ does not consider any external shear, there could be small changes in this relation due to the shear by the large scale flow and hence small changes in the 1/3 exponent of the $Nu \sim Ra$ scaling law, as a host of research on flux scaling in turbulent convection has shown. However the effect being quite small, as the difference in the flux scaling exponent shows, no noticeable difference in (6.23) would be felt in our range $Ra_w - Pr$ range.

7. Conclusions

In the present study of the dynamics of line plumes on the bottom plate in turbulent convection, we identified longitudinal motion, lateral merging and initiation as points as the predominant types of motion of these line plumes. The primary conclusions about these three types of motion of the plumes are as follows.

(*a*) The magnitude and scaling of the mean longitudinal motion along the plumes ($\overline{V_{sh}}$) at any instant is same as that of the large scale flow.

(*b*) The mean lateral merging velocity ($\overline{V_m}$) at any instant scales as the velocity scale ν/Z_w near the plate and are an order smaller than the large scale velocity.

(*c*) The mean time for initiation of plumes $\overline{t^*} \sim Z_w^2/\alpha$, the diffusive time scale near the plate.

These conclusions were obtained from experiments in thermally driven turbulent convection in air ($Pr = 0.7$), water ($Pr = 3.6$ to 5.3) and in concentration driven convection

in water ($Sc = 602$) over a six decade range of Rayleigh numbers ($10^5 < Ra_w < 10^{11}$). The velocities of the plumes were measured from visualisations in a horizontal plane close to the bottom plate, by laser scattering of smoke particles, electrochemical method and PLIF for the three Pr experiments respectively.

Among the three major types of motion of plumes, merging seems to occur in a large fraction of the area of the plate for the range of Ra_w and Pr in our experiments. The fraction of the length of the plumes that undergo merging (L_{pm}/L_p) reduced from about 90% at $Ra_w \approx 10^5$ to about 55% at $Ra_w \approx 10^9$; these fractions became larger with increase in Pr (5.7). We found that L_{pm}/L_p scales as $Ra_w^{-0.04}Pr^{0.1}$ (5.7). Interestingly, the fraction of the plume length affected by shear had an exact inverse dependence on Ra_w and Pr (5.3), so that the product of the lengths of plumes that merge and are affected by shear is a constant fraction of the square of the total plume length (5.11).

The plumes merge all over the planform with a range of velocities so that the instantaneous merging velocities (V_{mi}) show a distribution at any Ra_w and Pr. Such a distribution is partly caused by the spatially and temporally varying shear field near the plate due to the large scale flow, since shear reduces the merging velocities. We found that the distribution of merging velocities have a common log-normal distribution at all Ra_w and Pr; however the mean and standard deviations of the distributions increased with increase in Ra_w and decrease in Pr (§ 5.3.3). Plumes merged faster, with their merging velocities spread over increasing ranges, with increase in Ra_w and decrease in Pr. Significantly, each merging sequence of adjacent plumes occured with a constant velocity V_m at a location. As we show from a control volume balance, such constant V_m occurs since V_m is proportional to the average entrainment velocity ($\overline{V_h}$) at the sides of the plumes (6.5). During a merging cycle at a given Ra_w, the strength of two adjacent plumes remains constant, and hence $\overline{V_h}$ which is proportional to the plume rise velocities, too is a constant.

Using similarity solutions of Gebhart *et al.* (1970) for estimating $\overline{V_h}$ and relations for the mean plume spacing, to relate heat flux into the plumes to the heat flux into the plate, we obtained scaling laws for $\overline{V_m}$, the spatio-temporal mean merging velocities. $\overline{V_m} \sim \nu/Z_w$ (6.13), the appropriate velocity scale near the plate, where Z_w (1.2) is the relevant length scale near the plate in turbulent convection. The Reynolds number in terms of $\overline{V_m}$ and layer height H scaled as $Ra_w^{1/3}$ (6.15) or as the dimensionless flux Nu (6.23). The above relations also implied that $\overline{V_m}$ made dimensionless by the appropriate variables near the plate, in terms of the Reynolds number $Re_w = \overline{V_m}Z_w/\nu$ and Froude number $Fr_w^2/\beta\Delta T_w$, where $Fr_w = \overline{V_m}/\sqrt{gZ_w}$ remained invariant for a given fluid (6.18)(6.20).

We gratefully acknowledge the partial financial support by DST, Govt. of India under the grants SR/FST/ETII-017/2003 and SR/S3/MERC/028/2009 for this study. The experiments at $Pr = 0.74$ were conducted at DLR, Gottingen; we acknowledge the financial support of STAR programme of DAAD and IITM for these experiments. We are grateful to D. Schmeling, J. Bosbach, O. Shishkina and C. Wagner for their hospitality at Gottingen. BAP is grateful to J.H. Arakeri for his guidance for the experiments at $Sc = 602$, that were conducted at IISc, Bangalore.

Appendix A. Location of measurement vis-a-vis the boundary layer thicknesses.

The dotted line in figure 20 shows the height of the plane of measurement (h_m) against the natural convection velocity boundary layer thickness (δ_v) and the Prandtl-Blasius velocity boundary layer thickness (δ_{pb}). $h_m = 4$mm from the bottom plate for the $Pr =$

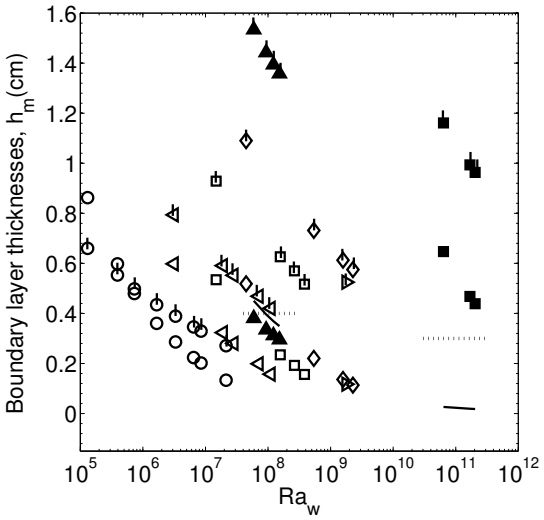

FIGURE 20. Variation of natural convection velocity boundary layer thickness δ_v and the Prandtl-Blasius velocity boundary layer thickness δ_{pb} with Ra_w. The symbols with vertical line show δ_{pb} while symbols without the vertical line show δ_v. The open symbols show the thermal convection experiments in water at $Pr = 3.6$ to 5.3 for the following layer heights; $\circ$, $H = 50$mm; $\triangleright$, $H = 100$mm; $\square$, $H = 150$mm; $\triangledown$, $H = 200$mm and $\diamond$, $H = 210$mm. $\blacktriangle$ and $\blacksquare$ indicate experiments at $Pr = 0.74$ and $Sc = 602$ respectively. The solid lines show the variation of δ, the natural convection thermal boundary layer thickness for $Pr = 0.74$ and $Sc = 602$; the horizontal dotted lines show the corresponding height of the plane of measurement h_m.

0.74 experiments and 3mm for the $Sc = 602$ experiments. Since the natural convection thermal boundary layer thickness $\delta \ll \delta_v$ as Pr is more than one, for the experiments in water at $3.6 < Pr < 5.3$, the dye formed on the plate is collected by the thermal boundary layers and accumulated at the plume base before being taken upwards by the plumes to be dispersed. The streaks that we see in these experiments are hence between δ and δ_v.

The symbols without a vertical line show

$$\delta_v = \left(\frac{C_1}{2}\right)^{2/5} \frac{H}{Ra_w^{1/3}} Pr^{\frac{4n_1+5}{10}} \tag{A 1}$$

at a horizontal distance of mean plume spacing $\overline{\lambda}$, as estimated from (A16) and (A11) of Puthenveettil *et al.* (2011), where $C_1 = 47.5$ and $n_1 = 0.1$. The solid lines show $\delta \sim \delta_v/\sqrt{Pr}$ for $Pr = 0.74$ and $Sc = 602$, as given by (A17) in Puthenveettil *et al.* (2011). δ_{pb} is shown by symbols with a vertical line, as estimated from

$$\frac{\delta_{pb}}{L} = \frac{0.483}{\sqrt{Re_L}}, \tag{A 2}$$

$$Re_L = 0.102 Ra^{0.447} Pr^{-0.7}, \tag{A 3}$$

based on the expectation that it is created by the large scale flow in this range (Ahlers, Grossman & Lohse 2009). The corresponding thermal boundary layer thickness will again be $1/\sqrt{Pr}$ of δ_{pb}. The figure shows that for all Pr, $h_m \ll \delta_{pb}$. For $Pr > 1$ experiments, $\delta < h_m < \delta_v$. For the $Pr < 1$ experiments, $\delta_v < h_m < \delta$ for the first two Ra_w and $h_m > \delta$ for the last two Ra_w. Our plane of measurement is not fixed relative to δ_v since

h_m is constant for each Pr experiment while δ_v changes due to change in Ra_w. We now look at the consequences of such a vertical location of the plane of measurement on the measured V_{sh}; the effects are expected to be negligible on $\overline{V_m}$ and $\overline{t^*}$.

Our $h_m \ll \delta_{pb}$. However, it would be incorrect to assume that that there is a steady Prandtl-Blasius boundary layer up to δ_{pb} within which there is a strong vertical gradient of horizontal velocities, which would strongly change the measured V_{sh} with small vertical shifts. This is because the reported vertical variation of the horizontal velocities (Xia, Lam & Zhou 2002), at least close to the plate, are the time averaged values of velocity contributions from a) plumes that are rising and horizontally moving, b) till a height of δ_v, from natural convection convection velocity boundary layers in between the plumes, and c) from the external large scale velocity in between plumes above δ_v. Due to the structure shown in figure 17(a), the external large scale velocity field on the side of the plumes is expected to extend from the center of the convection cell up to δ_v or δ, whichever is larger based on the value of Pr; i.e. to a height much lower than δ_{pb}.

Due to this, for the experiments where $h_m < \delta_v$, there is no longitudinal forcing by the large scale flow at the sides of the plumes since the velocity below δ_v is mostly perpendicular to the length of the plumes. Small changes in the height of measuring plane will not take the location out of δ_v and hence not change the observed longitudinal velocities. The question then arises as to how the longitudinal motion occurs in the plane of observation if there is no shear at the sides of the plumes in the plane of observation in these cases. Our guess is that the longitudinal motion occurs possibly due to the dragging of the plume region above this plane due to the large scale flow. However, this is just a surmise and we need far more investigations to understand the interaction of plumes and large scale flow.

For the $Pr = 0.74$ experiments, $\delta < h_m$ for the last two Ra_w; there is external shear at the sides of the plume in the plane of measurement. The characteristic vertical gradient of shear due to large scale flow in between the plumes will be of the order of $\partial V_{LS}/\partial z \sim V_{LS}/H$, since the vertical extent of large scale flow is from the center of the cell to δ_v and since $\delta_v \ll H$. The variation of δ in our range of Z_w (or Ra_w, since $Ra_w^{1/3} = H/Z_w$)is

$$\frac{\partial \delta}{\partial Z_w} \Delta Z_w \sim 1\text{mm} \tag{A 4}$$

small compared to H, the distance over which V_{LS} changes. The percentage change in longitudinal velocity due to measurement at a fixed location with respect to the bottom plate when Ra_w changes in our range, compared to that would occur if the measurement was at a fixed location relative to δ, would be

$$\frac{\Delta V_{LS}}{V_{LS}} \sim \left(\frac{\partial \delta}{\partial Z_w} \Delta Z_w \frac{V_{LS}}{H} \right) \frac{1}{V_{LS}} \sim \frac{\partial \delta}{\partial Z_w} \Delta Z_w \frac{1}{H} \sim 0.002. \tag{A 5}$$

The maximum percentage change in V_{LS} between the values at a fixed location relative to δ and the values at a fixed location relative to bottom is 0.2%, which is quite small; the error due to this difference is hence negligible.

In summary, for the thermal experiments in water, for the $Sc = 602$ experiments and for part of the $Pr = 0.74$ experiments, since the measuring plane is below δ_v and is not expected to go out of δ_v within the range of our experiments, there is no longitudinal shear due to large scale flow on the sides of the plume in this measuring plane; there is then no vertical gradients of such shear too. For the $Pr = 0.74$ experiments for which the measuring plane is above δ, change in shear from the value that would have occured at the same relative location with respect to δ in all experiments, is negligibly small.

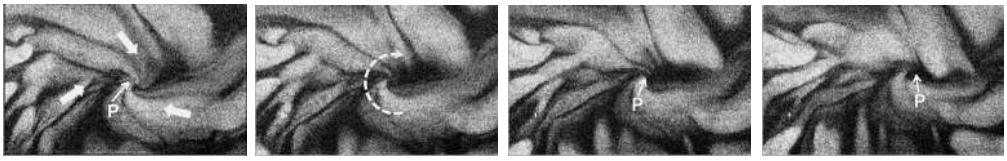

(a) (b) (c) (d)

FIGURE 21. (a) to (d), Swirling motion of plumes at $Pr = 0.74$, and $Ra_w = 2.54 \times 10^8$; (a), the filled arrows show the direction of shear while the dashed arrow shows the direction of swirling about the point P. The images are of size171mm×112mm and separated by 0.2 s.

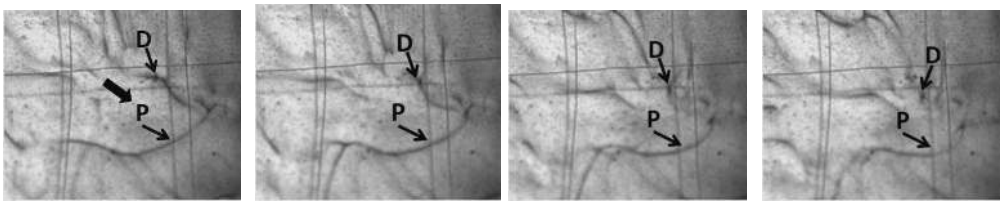

(a) (b) (c) (d)

FIGURE 22. (a) to (d), Lateral motion of plumes due to shear at $Pr = 3.6$, and $Ra_w = 2.27 \times 10^9$. The plume P moves laterally along the direction of shear shown by the filled arrow, identified by the motion of the feature marked by D. The images are of size 98mm×79mm and separated by 2 s.

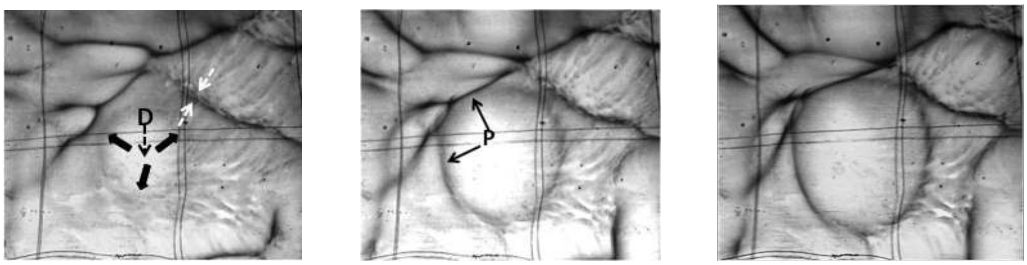

(a) $t = 0$ s (b) $t = 8$ s (c) $t = 14$ s

FIGURE 23. (a) to (d), Lateral plume motion due to local impingement of bulk flow at $Pr = 5.3$, and $Ra_w = 1.31 \times 10^5$. The filled arrows show the shear due to the downflow at D. The plumes P align at the outer periphery of the local shear. The dashed arrows show the direction of motion in the boundary layers between the plumes. The images are of size 157mm×135mm.

Appendix B. Miscellaneous motions

In addition to the three major class of motions described in § 3, there are other minor motions that occur not so frequently in the planforms. One of such motions is shown in figure 21 which occurs at the intersection of shear in the opposite directions. In figure 21(a) there is a shear directed downwards from the top left shown by the top filled arrow and shear upwards from the bottom right, shown by the bottom filled arrow. Intersection of these two shear streams causes the line plumes to start swirling about point P in the direction shown by the dashed arrow. The point P is usually also not stationary, as could be observed from figure 21 (a) to (d) where the location of P has shifted to the right. We find such swirling motion to occur more at lower Pr at a given Ra_w, possibly owing to the stronger shear at the lower Pr.

Even though plumes usually align along the direction of shear, as discussed in § 3.1,

there are situations where this does not occur. We sometimes find plumes whose both ends are connected to other plumes which are aligned along the direction of shear. Since such a plume is prevented from aligning by the plumes at its ends, it often moves laterally in the direction of shear without aligning along the direction of shear. Figure 22 shows such an instance where the plume marked by P moves laterally in the direction of shear without aligning in this direction. The filled arrow shows the direction of shear, which could be inferred by looking at the successive locations of the feature D in figures 22(a) to 22(d).

A similar situation of lateral plume motion in the presence of shear is also sometimes seen when the shear is not caused by the large scale flow, but by the local impingement of flows necessitated by rising local plume columns. Figure 23 shows such an instance where there is local impingement of flow at the point D which drives a shear in the directions shown by the filled arrows, thereby moving the plume P in a lateral direction. The shear could not be due to the external large scale flow, since it is not unidirectional as it is in the case of planforms discussed in § 3.1 and since there is no alignment of any of the plumes around the region of impingement.

Appendix C. Initial plume spacing during merging

It is possible that the linear variation of λ with t discussed in § 5.3.2, resulting in a constant V_m, is because we detect two line plumes as merging only when they come close together, so that a nonlinear variation appears linear due to the short range measurement. To verify whether this is so we study the variation of $\overline{\lambda_i}/\overline{\lambda}$ with Z_w for all the measurements of λ in figure 24. Here, $\overline{\lambda_i}$ is the first measurement of the plume spacing measured in each plume merging sequence, averaged over all such measurements at the same Ra_w. $\overline{\lambda}$ is the critical plume spacing given by Theerthan & Arakeri (1998) and Puthenveettil & Arakeri (2005) as,

$$\overline{\lambda} = C_1 Pr^{n_1} Z_w, \tag{C 1}$$

where $C_1 = 47.5$ and $n_1 = 0.1$. The figure shows that all the measurements of merging plumes were conducted on plumes that were separated by an initial spacing smaller than $\overline{\lambda}$. As we mentioned in § 3.2, only plumes closer than the critical spacing seems to merge, others fade away or are swept along their length by the shear. The dotted line in the figure has a slope of -1 implying that $\overline{\lambda_i}$ is not a function of Z_w. Since $\overline{\lambda_i}/\overline{\lambda}$ fall approximately on the same line for the experiments at $Sc = 602$ and the thermal experiments in water, $\overline{\lambda_i}$ is also approximately independent of Pr for these two experiments. Examination of the data showed us that all the $\overline{\lambda_i}$ are approximately equal to 5 mm, except for $Pr = 0.74$ where it is about 2.5 cm.

Appendix D. Error in V_{sh}, V_m and $\overline{t^*}$.

The error in V_m,

$$\sigma_{V_m} = \sigma_{\lambda/2}\sqrt{\frac{N}{\Delta}}, \tag{D 1}$$

where, $\sigma_{\lambda/2} = \frac{1}{N-2}\sum_{i=1}^{N}(\lambda_i/2 - \lambda_f)^2$, $\lambda_i/2$ is half the measured value of λ at each time t_i, λ_f the corresponding value from the fit between $\lambda_i/2$ and t_i, N is the number of

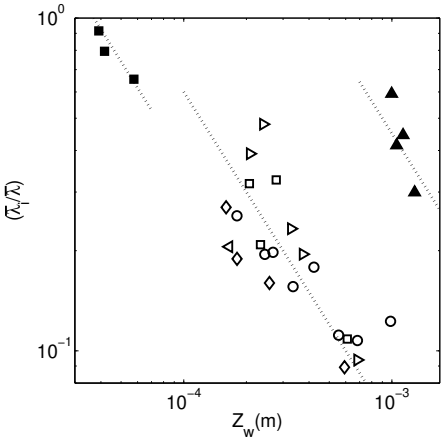

FIGURE 24. Variation with Rayleigh number of the initial plume spacing for merging sequences, averaged over their range at a given Ra_w and normalised by the mean plume spacing at the same Ra_w. The open symbols indicate thermal convection experiments in water for $Pr = 3.6$ to 5.3 for the following layer heights; ○, $H = 50$mm; ▷, $H = 100$mm; □, $H = 150$mm; ▽, $H = 200$mm and; ◇, $H = 210$mm. ▲, $Pr = 0.73, H = 500$mm; ■, $Sc = 602, H = 230$mm. $---, 0.0005Ra_w^{1/3}$.

measured λ and

$$\Delta = N\sum_{i=1}^{N} t_i^2 - \left(\sum_{i=1}^{N} t_i\right)^2 . \qquad \text{(D 2)}$$

Figure 16 shows the error bars corresponding to $\pm 3\sigma_{V_m}$, at the maximum and the minimum of the locational means V_m, at the Ra_w at which the range of V_m are shown. The maximum error in V_m is less than 10.2% of the value of V_m itself at $Ra_w = 6.39 \times 10^{10}$ at $Sc = 602$; similar maximum errors were obtained from the other Pr data. The estimation of V_m is hence statistically significant and sufficiently accurate. The error in V_m is less than 24% of the range of V_m at the corresponding Ra_w for $Pr = 0.74$, $< 30\%$ of the range at $Pr = 3.6$ and $< 40\%$ of the range at $Sc = 602$ showing that the error does not preclude us from estimating the approximate range of variation of V_m over the planform due to physical reasons.

Similar to the case of V_m, the error in the locational mean of V_{sh}, $\sigma_{V_{sh}}$ is calculated at each location, using relations similar to (D 1) and (D 2). Figure 11(a) shows the $\pm 3\sigma_{V_{sh}}$ as the error bar located on the maximum and the minimum V_{sh} at the Ra_w at which the range of V_{sh} is shown. The maximum of $3\sigma_{V_{sh}}/V_{sh}$ was about 9.7%, with most of the values being of the order of 2%, showing sufficiently accurate estimate of the locational mean. The maximum $3\sigma_{V_{sh}}$ was less that 16.6% of the range of the locational mean at the same Ra_w, with most of the values being about 6% of the corresponding range, showing that the error in locational mean does not prevent us from estimating the range of variation of the locational mean across the planform.

The error bars in figure 13 show the error in $\overline{t^*}$ due to finite sample size N, calculated as a precision limit $p = 2\sigma_{t^*}/\sqrt{N}$; the maximum error in the mean is for $Ra_w = 2.65 \times 10^8$ for water which is at 12% of the mean, with errors for other $Ra_w - Pr$ combinations being around 5%, implying sufficient accuracy and statistical significance for the measurements. Another theoretical upper limit of error could be obtained by considering that the first and last frames over which t^* is measured could be at most in error by one frame. The estimated error in t^* from such an estimate shows that the maximum error is 15.6% at

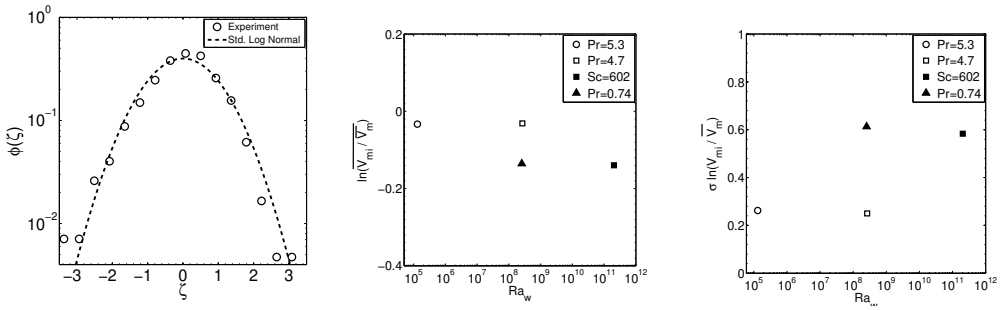

(a) (b) (c)

FIGURE 25. (a), The common probability density function of the logarithm of the dimensionless plume merging velocities in their standardised form $\zeta = (\ln(V_{mi}/\overline{V_m}) - \overline{\ln(V_{mi}/\overline{V_m})})/\sigma \ln(V_{mi}/\overline{V_m})$ at all Ra_w and Pr; (b), Variation of the mean of the logarithm of the dimensionless plume merging velocities with Ra_w; (c), Variation of the standard deviation of the logarithm of the dimensionless plume merging velocities

$Ra_w = 2.54 \times 10^8$ for air, with most of the errors for other $Ra_w - Pr$ being at around 5%.

Appendix E. Common PDF of merging velocities

The general probability distribution function of plume merging velocities is obtained by combining the merging velocity data, in the form of ζ, for all the Ra_w and Pr. Figure 25(a) shows such a PDF plot obtained from 1120 data points for the data shown in figure 15. The variation of the standardising parameters $\overline{\ln(V_{mi}/\overline{V_m})}$ and $\sigma \ln(V_{mi}/\overline{V_m})$ are shown in figures 25(b) and 25(c). The unfilled symbols have a constant value of $\overline{\ln(V_{mi}/\overline{V_m})} \approx -0.025$ while the filled symbols have a value about -0.14. Similarly, $\sigma \ln(V_{mi}/\overline{V_m}) \approx 0.25$ for the unfilled symbols while it is equal to 0.6 for the filled symbols. Studying figure 15, we observe that the pdf of the filled symbols, which are either at a much larger Ra_w or a much smaller Pr than the water experiments at $Pr \approx 5$, have a noticeable asymmetry with a larger probability of finding the lower than mean values of V_{mi} than the higher than mean values. This asymmetry lowers the $\overline{\ln(V_{mi}/\overline{V_m})}$ and increases the $\sigma \ln(V_{mi}/\overline{V_m})$ for the filled symbols, seen respectively in figure 25(b) and 25(c), when compared to the unfilled symbols. Shear increases with increase in Ra_w and decrease in Pr, and shear decreases the merging velocities. Hence at larger Ra_w and lower Pr we expect a higher probability of occurrence of V_{mi} smaller than the mean. Similarly, since increase in shear also increases the range of V_{mi} we expect $\sigma \ln(V_{mi}/\overline{V_m})$ to be higher at higher Ra_w and lower Pr.

Appendix F. Relation for Q_p

Equation (6.8) is for a single plume above a heated line source, in the case of convection over a hot surface, we need to relate the heat flux q from the plate to the strength of the line source Q_p of individual plumes in (6.10). The heat from the plate is transferred to the boundary layers on both sides of each of the plumes, which then input this heat to the base of each of the plume. The boundary layers, which become unstable at a mean distance of $\overline{\lambda}$, cover the plate. Hence, we assume that the total heat carried away by all the plumes from any area A on the plate at any instant is equal to the total heat supplied

by the plate in that area. Numerical studies by Shishkina & Wagner (2008) have shown that this assumption is valid.

Q_p in (6.10) is also the heat transported by the plume per unit length at any height, since the total heat transported by the plume is constant at any height. Now, if L_p is the total length of all the plumes in an area A of the plate, then equating the heat carried away by the plumes in an area A to the heat supplied by the plate in the same area A implies,

$$Q_p L_p = qA. \tag{F 1}$$

Since

$$L_p = A/\overline{\lambda}, \tag{F 2}$$

as shown by Puthenveettil *et al.* (2011),

$$Q_p = q\overline{\lambda}. \tag{F 3}$$

q in (F 3) could now be written in terms of $\overline{\lambda}$ to obtain a relation between Q_p, $\overline{\lambda}$ and fluid properties. Using the expression for Townsend's near-wall length scale,

$$Z_o = \left(\frac{\alpha^3 \rho C_p}{g\beta q}\right)^{1/4} \tag{F 4}$$

and the relation,

$$\frac{\overline{\lambda}}{Z_o} = C_2 Pr^{n_2}, \tag{F 5}$$

(Puthenveettil, Gunasegarane, Yogesh, Schmeling, Bosbach & Arakeri 2011), where, $C_2 = 31$ and $n_2 = 0.345$, along with (F 3), we get

$$Q_p = (C_2 Pr^{n_2})^4 \frac{\rho C_p}{g\beta} \left(\frac{\alpha}{\overline{\lambda}}\right)^3. \tag{F 6}$$

REFERENCES

Ahlers, G., Bodenschatz, E., Funfschilling, D., Grossmann, S., He, X., Lohse, D., Stevens, R. J. A. M. & Verzicco, R. 2012 Logarithmic temperature profiles in turbulent Rayleigh-Bénard convection. *Phys. Rev. Lett.* **109**, 114501.

Ahlers, G., Grossman, S. & Lohse, D. 2009 Heat transfer and large-scale dynamics in turbulent Rayleigh-Bénard convection. *Rev. Mod. Phys* **81**, 503.

Baker, J. D. 1966 A technique for the precise measurement of small flow velocities. *J.Fluid Mech.* **26** (3), 573–575.

Bosbach, J., Weiss, S. & Ahlers, G. 2012 Plume fragmentation by bulk interactions in turbulent Rayleigh-Bénard convection. *Phs. Rev. Let.* **108**, 054501.

Deardorff, J. 1970 Convective velocity and temperature scales for the unstable planetary boundary layer and for Rayleigh convection. *Jl. Atmos. Sci.* **27**, 1211–1213.

Funfschilling, D. & Ahlers, G. 2004 Plume motion and large scale circulation in a cylindrical Rayleigh-Bénard cell. *Phys.Rev.Lett.* **92(19)** (194502).

Gebhart, B., Pera, L. & Schorr, A. W. 1970 Steady laminar natural convection plume above a horizontal line heat source. *Intl J. Heat Mass Transfer* **13**, 161–171.

Grossman, S. & Lohse, D. 2002 Prandtl and rayleigh number dependence of the reynolds number in turbulent convection. *Phys. Rev. E* **66**, 016305.

Gunasegarane, G. S. 2014 Structure and dynamics of plumes in turbulent convection. PhD thesis, Dept. of Applied Mechanics, IIT Madras.

Haramina, T. & Tilgner, A. 2004 Coherent structures in boundary layers of Rayleigh-Bénard convection. *Phys. Rev. E* **69** (056306).

Hogg, J. & Ahlers, G. 2013 Reynolds number measurements for low-Prandtl-number turbulent convection of large aspect-ratio samples. *Jl. Fluid. Mech.* Submitted.

Howard, L. N. 1964 Convection at high Rayleigh number. In *Proc. 11th Int. congress applied mechanics, Munich* (ed. H. Gortler), pp. 1109–1115.

Husar, R. B. & Sparrow, E. M. 1968 Patterns of free convection flow adjacent to horizontal heated surfaces. *Intl J. Heat Mass Transfer* **11**, 1208–1211.

Lam, S., Shang, X., Zhou, S. & Xia, K. 2002 Prandtl number dependence of the viscous boundary layer and the Reynolds numbers in Rayleigh number convection. *Phys. Rev. E* **65**, 066306.

Pera, L. & Gebhart, B. 1973 On the stability of natural convection boundary layer flow over horizontal and slightly inclined surfaces. *Intl J.Heat Mass Transfer* **16**, 1147–1163.

Puthenveettil, B. A., Ananthakrishna, G. & Arakeri, J. H. 2005 Multifractal nature of plume structure in high Rayliegh number convection. *J. Fluid Mech.* **526**, 245–256.

Puthenveettil, B. A. & Arakeri, J. H. 2005 Plume structure in high Rayleigh number convection. *J. Fluid Mech.* **542**, 217–249.

Puthenveettil, B. A. & Arakeri, J. H. 2008 Convection due to an unstable density difference across a permeable membrane. *J. Fluid Mech.* **609**, 139–170.

Puthenveettil, B. A., Gunasegarane, G. S., Yogesh, K. A., Schmeling, D., Bosbach, J. & Arakeri, J. H. 2011 Length of near-wall plumes in turbulent convection. *J.Fluid Mech.* **685**, 335–364.

Qiu, X.-L. & Xia, K.-Q. 1998 Spatial structure of the viscous boundary layer in turbulent convection. *Phys. Rev. E* **58**, 5816–5820.

Ramareddy, G. V. & Puthenveettil, B. A. 2011 The $Pe \sim 1$ regime of convection across horizontal permeable membrane. *J.Fluid Mech.* **679**, 476–504.

Schneider, W. 1981 Flow induced by jets and plumes. *J. Fluid Mech.* **108**, 55–65.

Shishkina, O. & Thess, A. 2009 Mean temperature profiles in turbulent RayleighBénard convection of water. *J. Fluid. Mech.* **633**, 449–460.

Shishkina, O. & Wagner, C. 2008 Analysis of sheet-like thermal plumes in turbulent Rayleigh-Bénard convection. *J. Fluid Mech.* **599**, 383–404.

Spangenberg, W. G. & Rowland, W. G. 1961 Convective circulation in water induced by evaporative cooling. *Phys. Fluids* **4** (6), 743–750.

Theerthan, S. A. & Arakeri, J. H. 1998 A model for near wall dynamics in turbulent Rayleigh-Bénard convection. *J. Fluid Mech.* **373**, 221–254.

Theerthan, S. A. & Arakeri, J. H. 2000 Planform structure and heat transfer in turbulent free convection over horizontal surfaces. *Phys. Fluids* **12**, 884–894.

Xia, K. Q., Lam, S. & Zhou, S. Q. 2002 Heat flux measurement in high Prandtl number turbulent Rayleigh-Bénard convection. *Phys. Rev. Lett.* **88(6)** (064501).

Zhou, Q. & Xia, K. Q. 2010 Physical and geometrical properties of thermal plumes in turbulent Rayleigh-Bénard convection. *New J. Phys.* **12** (075006).

Zocchi, G., Moses, E. & Libchaber, A. 1990 Coherent structures in turbulent convection, an experimental study. *Physica A* **166**, 387–407.